



Title	Quantitative Imaging Reveals Distinct Contributions of SnRK2 and ABI3 in Plasmodesmatal Permeability in <i>Physcomitrella patens</i>
Author(s)	Tomoi, Takumi; Kawade, Kensuke; Kitagawa, Munenori; Sakata, Yoichi; Tsukaya, Hirokazu; Fujita, Tomomichi
Citation	Plant and Cell Physiology, 61(5), 942-956 <a href="https://doi.org/10.1093/pcp/pcaa021">https://doi.org/10.1093/pcp/pcaa021</a>
Issue Date	2020-05
Doc URL	<a href="http://hdl.handle.net/2115/81128">http://hdl.handle.net/2115/81128</a>
Rights	This is a pre-copyedited, author-produced version of an article accepted for publication in Plant and cell physiology following peer review. The version of record Plant Cell Physiol (2020) 61 (5): 942–956 is available online at: <a href="https://doi.org/10.1093/pcp/pcaa021">https://doi.org/10.1093/pcp/pcaa021</a> .
Type	article (author version)
Additional Information	There are other files related to this item in HUSCAP. Check the above URL.
File Information	Plant Cell Physiol.61-5_942-956.pdf



[Instructions for use](#)

1 **Article title**

2 Quantitative imaging reveals distinct contributions of SnRK2 and ABI3 in plasmodesmatal  
3 permeability in *Physcomitrella patens*

4

5 **Author names**

6 Takumi Tomoi, Kensuke Kawade, Munenori Kitagawa, Yoichi Sakata, Hirokazu Tsukaya, and  
7 Tomomichi Fujita

8

9 **Corresponding authors**

10 Kensuke Kawade; [kawa-ken@nibb.ac.jp](mailto:kawa-ken@nibb.ac.jp); Phone: +81 (0)564 59 5883

11 Tomomichi Fujita; [tfujita@sci.hokudai.ac.jp](mailto:tfujita@sci.hokudai.ac.jp); Phone: +81 (0)11 706 2740

12

13

14

15 Six Figures

16 One Supplementary Table

17 Six Supplementary Figures

18

19 **Short title**

20 ABA signaling for plasmodesmatal permeability

21

22 **Article title**

23 Quantitative imaging reveals distinct contributions of SnRK2 and ABI3 in plasmodesmatal  
24 permeability in *Physcomitrella patens*

25

26 **Author names and affiliations**

27 Takumi Tomoi<sup>a,b</sup>, Kensuke Kawade<sup>b,c,d,1</sup>, Munenori Kitagawa<sup>e</sup>, Yoichi Sakata<sup>f</sup>, Hirokazu  
28 Tsukaya<sup>b,g</sup>, and Tomomichi Fujita<sup>h,1</sup>

29

30 <sup>a</sup>Graduate School of Life Science, Hokkaido University, Kita10 Nishi8, Kita-ku, Sapporo,  
31 Hokkaido 060-0810, Japan

32 <sup>b</sup>Exploratory Research Center on Life and Living Systems (ExCELLS), 5-1 Higashiyama,  
33 Myodaiji, Okazaki, Aichi 444-8787, Japan

34 <sup>c</sup>National Institute for Basic Biology, 38 Nishigonaka, Myodaiji, Okazaki, Aichi 444-8585,  
35 Japan

36 <sup>d</sup>Department of Basic Biology, School of Life Science, Graduate University for Advanced  
37 Studies (SOKENDAI), 38 Nishigonaka, Myodaiji, Okazaki, Aichi 444-8585, Japan

38 <sup>e</sup>Cold Spring Harbor Laboratory, 1 Bungtown road, Cold Spring Harbor, New York 11724,  
39 USA

40 <sup>f</sup>Department of Bioscience, Tokyo University of Agriculture, 1-1-1 Sakuragaoka, Setagaya-ku,  
41 Tokyo 156-8502, Japan

42 <sup>g</sup>Department of Biological Sciences, Graduate School of Science, The University of Tokyo,  
43 7-3-1 Hongo, Bunkyo-ku, Tokyo 113-0033, Japan

44 <sup>h</sup>Department of Biological Sciences, Faculty of Science, Hokkaido University, Kita10 Nishi8,  
45 Kita-ku, Sapporo, Hokkaido 060-0810, Japan

46

47

48 **One-sentence summary**

49 A protein kinase and a transcription factor are an essential and a promotive factor in the  
50 regulation of cell-to-cell connectivity in response to plant stress hormone abscisic acid.

51

52 **Author contributions**

53 T.T. and T.F. conceived the project. T.T. and K.K. designed the study. H.T. and T.F. directed  
54 the study. T.T. performed all experiments and analyzed the data. M.K. and Y.S. provided  
55 materials. T.T., K.K., and T.F. wrote the manuscript with input from co-authors.

56

57 **Funding information**

58 This work was supported by the BIO-NEXT project from the Exploratory Research Center on  
59 Life and Living Systems (ExCELLS) (K.K. and H.T.), a Grant-in-Aid for Scientific Research  
60 on Innovative Areas from the Japan Society for the Promotion of Science (25113002 to H.T.),  
61 Grant-in-Aid for Challenging Exploratory Research from Japan Society for the Promotion of  
62 Science (JSPS) (18H04829 to T. F.), and Grant-in-Aid for Scientific Research on Innovative  
63 Areas from JSPS (25650089 to T. F.).

64

65 **Email address of Author for Contact**

66 <sup>1</sup>Corresponding authors

67 Kensuke Kawade; [kawa-ken@nibb.ac.jp](mailto:kawa-ken@nibb.ac.jp); Phone: +81 (0)564 59 5883

68 Tomomichi Fujita; [tfujita@sci.hokudai.ac.jp](mailto:tfujita@sci.hokudai.ac.jp); Phone: +81 (0)11 706 2740

69

70

71 **Abstract**

72 Cell-to-cell communication is tightly regulated in response to environmental stimuli in plants.

73 We previously used photoconvertible fluorescent protein Dendra2 as a model reporter to study

74 this process. This experiment revealed that macromolecular trafficking between protonemal

75 cells in *Physcomitrella patens* is suppressed in response to abscisic acid (ABA). However, it

76 remains unknown what and how ABA signaling components contribute to this suppression.

77 Here, we showed that ABA signaling components SUCROSE NON-FERMENTING  
78 1-RELATED PROTEIN KINASE 2 (PpSnRK2) and ABA INSENSITIVE 3 (PpABI3) play  
79 roles as an essential and a promotive factor, respectively in regulating ABA-induced  
80 suppression of Dendra2 diffusion between cells (ASD). Our quantitative imaging analysis  
81 revealed that disruption of *PpSnRK2* resulted in defective ASD onset itself, whereas  
82 disruption of *PpABI3* caused an 81-min delay in initiation of ASD. Live-cell imaging of  
83 callose deposition using aniline blue staining showed that, despite this onset delay, callose  
84 deposition on cross walls remained constant in the *PpABI3* disruptant, suggesting that  
85 PpABI3 facilitates ASD in a callose-independent manner. Given that ABA is an important  
86 phytohormone to cope with abiotic stresses, we further explored cellular physiological  
87 responses. We found that acquisition of salt stress tolerance is promoted by PpABI3 in a  
88 quantitative manner similar to ASD. Our results suggest that PpABI3-mediated ABA  
89 signaling may effectively coordinate cell-to-cell communication during acquisition of salt  
90 stress tolerance. This study will accelerate quantitative study for ABA signaling mechanism  
91 and function in response to various abiotic stresses.

92

93

#### 94 **KEYWORDS**

95 abscisic acid signaling, cell-to-cell communication, *Physcomitrella patens*, quantitative  
96 imaging analysis, salt stress tolerance

97

98

#### 99 **Introduction**

100 The phytohormone ABA plays a pivotal role in overcoming water-deficit stress conditions.  
101 Extensive molecular analyses have identified core components of ABA signaling in  
102 angiosperms which include an ABA receptor pyrabactin resistance 1-like (PYL) (also known  
103 as PYR or RCAR) (Ma et al., 2009; Park et al., 2009), a positive regulator of ABA signaling  
104 SnRK2 (Li et al., 2000; Mustilli et al., 2002; Yoshida et al., 2002), and its negative regulator  
105 of group A protein phosphatase type 2C (PP2C) (Umezawa et al., 2009; Vlad et al., 2009).

106 Under non-stressed conditions, PP2C interacts and suppress SnRK2 kinase activity (Yoshida  
107 et al., 2019). Once plants are exposed to water-deficit stress conditions, ABA binds to PYL  
108 receptor, which then inactivates PP2C to release SnRK2. This mechanism induces a  
109 SnRK2-mediated phosphorylation relay to activate the ABA signaling (Yoshida et al., 2019).  
110 Although details of molecular mechanisms are partially different, these ABA signaling  
111 components are highly conserved in basal land plants bryophytes such as moss *Physcomitrella*  
112 *patens* and liverwort *Marchantia polymorpha* (Khandelwal et al., 2010; Komatsu et al., 2013;  
113 Saruhashi et al., 2015; Stevenson et al., 2016; Eklund et al., 2018; Shinozawa et al., 2019).

114 Because plasmodesmata (PD) are cytoplasmic channels which transverse the cell walls  
115 to allow cell-to-cell communication, PD permeability is one of the critical elements to  
116 determine the extent of cell-to-cell communication. Interestingly, in addition to various  
117 phytohormones, downstream output of the ABA signaling is involved in the regulation of  
118 cell-to-cell communication by modulating callose deposition at PD in angiosperms (Han and  
119 Kim, 2016; Amsbury et al., 2018; Tylewicz et al., 2018; Wu et al., 2018). For example, in  
120 response to shorter photoperiods, PD permeability in shoot apices of *Populus* is reduced  
121 through the ABA signaling by formation of callosic sphincters to maintain bud dormancy  
122 (Tylewicz et al., 2018). The effect of ABA is compromised by expression of a dominant  
123 mutant allele *PP2C* of *Arabidopsis thaliana* *ABA INSENSITIVE 1 (abi1-1)* (Tylewicz et al.,  
124 2018). This *abi1-1* phenotype was rescued by overexpression of *PD-LOCATED PROTEIN 1*  
125 (*PDLP1*), a type I membrane-receptor protein family (Tylewicz et al., 2018). Given that the  
126 PDLP-mediated callose deposition is likely to occur through direct interactions with  
127 *CALLOSE SYNTHASE (CALS) 10/GLUCAN SYNTHASE LIKE (GSL) 8* (Saatian et al., 2018),  
128 the PDLPs are important regulators for PD permeability through callose deposition in  
129 angiosperms. We recently reported that intercellular Dendra2 movement through PD in *P.*  
130 *patens* protonemal cells is suppressed by ABA treatment (Kitagawa et al., 2019).  
131 Transmission electron microscopy (TEM) revealed that ABA treatment decreased PD aperture  
132 size from 38 nm to 29 nm but had little effect on PD density (Kitagawa et al., 2019). Aniline  
133 blue staining indicated, however, that there is negligible change in callose deposition on cross  
134 walls after ABA treatment during decrease in PD permeability (Kitagawa et al., 2019). These

135 data suggest that the ABA-induced suppression of intercellular Dendra2 movement is likely to  
136 occur in a callose-independent fashion. Furthermore, genome database search identified no  
137 *PDLP* orthologous genes in *P. patens* (Lee, 2014; Brunkard and Zambryski, 2017). Therefore,  
138 it is of great interest to unravel how, in the absence of functional PDLPs the ABA  
139 signaling-mediated PD permeability is regulated in *P. patens*.

140 Photoconvertible fluorescent proteins such as Dendra2 and DRONPA have been used to  
141 analyze PD permeability. This quantitative approach revealed that, for example, in *A. thaliana*  
142 roots different cell types have different PD permeability, and their sensitivities in response to  
143 flagellin, low temperature and salicylic acid also differ (Wu et al., 2011; Gerlitz et al., 2018).  
144 In addition, we previously established an experimental setup to visualize and analyze  
145 intercellular Dendra2 movement in protonemal cells of *P. patens* (Kitagawa and Fujita, 2013;  
146 Kitagawa and Fujita, 2015), and found a phenomenon of ABA-induced suppression of  
147 Dendra2 movement between cells (ASD) (Kitagawa et al., 2019). However, due to a lack of  
148 quantitative characterization of the Dendra2 movement, its biophysical property such as  
149 diffusivity is still unclear. This prevents us from quantitatively dissecting the contributions of  
150 ABA signaling components on the regulation of PD permeability. In this study, we examined  
151 how the ABA signaling components *PpSnRK2* and *PpABI3* are involved in ASD by  
152 quantitatively characterizing the Dendra2 movement between protonemal cells through PD.  
153 Our analysis revealed different contributions of these two components on the regulation of PD  
154 permeability in response to ABA. Furthermore, we detected a delay in the ASD initiation in a  
155 *PpABI3* disruptant and that this delay is quite similar to the timescale required for salt stress  
156 tolerance acquisition in response to ABA. Based on these results, we discuss a possible  
157 function of *PpABI3* in coordinating the rapid initiation of ASD and salt stress tolerance  
158 acquisition in *P. patens*.

159

160

## 161 **Results**

### 162 **Overexpression of *PpABI1A*<sup>G333D</sup>, *PpSnRK2A*, and *PpABI3A* impacted on cellular growth** 163 **and morphology**

164 In response to the ABA treatment, protonemal cells of moss including *P. patens* exhibit drastic  
165 morphological changes and growth suppression and eventually differentiate into brood cells  
166 (or brachyocytes) (Schnepf and Reinhard, 1997; Rowntree et al., 2007; Komatsu et al., 2009;  
167 Amagai et al., 2018). We observed a similar morphological changes in our transgenic line  
168 *ProEF1α:D2*, which constitutively expresses *Dendra2* (*D2*) under the control of an *EF1α*  
169 promoter. ABA treatment on the *ProEF1α:D2* inhibited cell growth but cell division was  
170 unaffected, and this resulted in the formation of round-shape cells like brood cells in their  
171 apices and slightly swollen cells in their basal regions (Fig. 1A). To examine whether these  
172 ABA-induced phenotypes requires the ABA signaling components, we constitutively  
173 overexpressed *PpABI1A<sup>G333D</sup>* in the *ProEF1α:D2* background  
174 (*PpABI1A<sup>G333D</sup>OX/ProEF1α:D2*). The *PpABI1A<sup>G333D</sup>* allele harbors a hypermorphic mutation  
175 which phenocopies the *A. thaliana abil-1* allele that acts as a negative regulator in ABA  
176 signaling (Koornneef et al., 1984; Eklund et al., 2018). We observed that cellular phenotypes  
177 in *PpABI1A<sup>G333D</sup>OX/ProEF1α:D2* did not show significant difference between dimethyl  
178 sulfoxide (DMSO) control and ABA-treated samples (Fig. 1B). This indicates that the  
179 *PpABI1A<sup>G333D</sup>* negatively impacted on the ABA signaling in *P. patens*, similar to that in *A.*  
180 *thaliana*.

181 We next examined whether the ABA-induced cellular phenotypes are reproducible by  
182 inducible overexpressions of *PpSnRK2A* and *PpABI3A* in the *ProEF1α:D2* background  
183 (*PpSnRK2AiOX/ProEF1α:D2* and *PpABI3AiOX/ProEF1α:D2*). Transcripts of *PpSnRK2A* and  
184 *PpABI3A* were readily detectable 24 hours after β-estradiol treatment (Supplemental Fig. S1,  
185 A-D). Expression levels of the transgenic *PpSnRK2A* and *PpABI3A* were much higher than  
186 the endogenous expression levels of *PpSnRK2A-D* and *PpABI3A-C* after ABA treatment  
187 (Supplemental Fig. S1, E-H). We confirmed that its cellular growth and morphology in the  
188 *ProEF1α:D2* were normal either in the absence or presence of β-estradiol (Fig. 1C). We  
189 observed that the growth of protonemal cells in the *PpSnRK2AiOX/ProEF1α:D2* ceased and  
190 exhibited swollen phenotypes upon β-estradiol treatment (Fig. 1D). On the other hand, the  
191 *PpABI3AiOX/ProEF1α:D2* primarily showed growth suppression with little morphological  
192 changes (Fig. 1E). We thus demonstrated that inducible expressions of either *PpSnRK2A* or



193 *PpABI3A* in the *PpSnRK2AiOX/ProEF1α:D2* and *PpABI3AiOX/ProEF1α:D2* lines can  
194 partially phenocopies the ABA-induced morphological changes (Fig. 1, C-E).

195

### 196 **Overexpression of *PpABI1A*<sup>G333D</sup>, *PpSnRK2A*, and *PpABI3A* influences intercellular** 197 **Dendra2 movement in protonemal cells**

198 Since overexpression of *PpABI1A*<sup>G333D</sup>, *PpSnRK2A*, and *PpABI3A* impacted on the cellular  
199 growth and morphology, we analyzed Dendra2 movement between protonemal cells in  
200 *PpABI1A*<sup>G333D</sup>*OX/ProEF1α:D2*, *PpSnRK2AiOX/ProEF1α:D2*, and  
201 *PpABI3AiOX/ProEF1α:D2* to clarify contribution of these components on suppression of the  
202 Dendra2 movement. In this system, intensity of the photoconverted Dendra2 red signal in  
203 *ProEF1α:D2* decreased as the Dendra2 move away from the original cell over time in a  
204 PD-mediated manner (Fig. 2A) (Kitagawa and Fujita, 2013; Kitagawa et al., 2019). Upon  
205 ABA treatment, the Dendra2 intensity remained constant in the original cell, suggesting that  
206 Dendra2 movement to neighboring cells was inhibited (Fig. 2A).

207 In the *PpABI1A*<sup>G333D</sup>*OX/ProEF1α:D2*, although the Dendra2 movement was seemingly  
208 suppressed upon ABA treatment as compared to the DMSO control, intercellular Dendra2  
209 movement was still observed (Fig. 2B), suggesting a partial contribution of *PpABI1* on the  
210 suppression of Dendra2 movement between cells. On the other hand, the Dendra2 movement  
211 was fully suppressed in *PpSnRK2AiOX/ProEF1α:D2* and *PpABI3AiOX/ProEF1α:D2* upon  
212 inducible overexpression of *PpSnRK2A* and *PpABI3A*, as compared to the corresponding  
213 DMSO controls (Fig. 2, C-E). These observations indicate that inducible overexpression of  
214 either *PpSnRK2A* or *PpABI3A* is sufficient to suppress the intercellular Dendra2 movement  
215 even in the absence of ABA treatment.

216

### 217 **Quantification workflow to analyze Dendra2 movement between protonemal cells in** 218 **response to ABA**

219 We next established a method to quantitatively analyze the kinetics of Dendra2 intensity over  
220 time based on a time-lapse Dendra2 imaging system reported previously (Kitagawa and Fujita,  
221 2013). To rule out the possibility that disappearance of the Dendra2 intensity was due to

222 proteolytic protein turnover, we tracked the Dendra2 intensity in the presence of MG-132, a  
223 proteasome inhibitor. We found that the Dendra2 intensity in protoplasts was unchanged over  
224 the course of 720 min, both in MG-132-treated and DMSO control (Supplemental Fig. S2).  
225 This indicated that proteolytic degradation of Dendra2 is negligible for at least 720 min. In  
226 addition, we analyzed the Dendra2 intensity in the neighboring cells of the photoconverted  
227 cells. As the Dendra2 intensity was decreased in the original 12th cell, the increase in the  
228 Dendra2 intensity in the neighboring 11th and 13th cells was detected (Supplemental Fig. S3).  
229 Thus our data suggest that the decrease in the Dendra2 intensity in the original cell was due to  
230 the intercellular movement between the protonemal cells. In our previous report (Kitagawa  
231 and Fujita, 2013), directional movement of the Dendra2 towards apical side of protonemata  
232 was observed when protonemal cells were grown under the light condition but not under the  
233 dark condition. Consistently, in the time-lapse imaging under the dark condition in this study,  
234 directional bias of the Dendra2 movement was not found (Supplemental Fig. S3). It is also  
235 noted that the decrease in the Dendra2 intensity in the 11th and 13th neighboring cells was  
236 detectable over time, probably because the Dendra2 was diffused further.

237 We furthermore determined that this intercellular Dendra2 movement can be defined as a  
238 simple diffusion process because the kinetics of the Dendra2 intensity in the photoconverted  
239 cell was well fitted with a single exponential function (Fig. 3, A and B). This indicates that the  
240 intercellular Dendra2 mobility is characterized by two parameters, a time constant ( $\tau$ ) and an  
241 immobile fraction ( $B$ ). The  $\tau$  represents intercellular diffusivity of the Dendra2 through PD,  
242 and the  $B$  refers to the ratio of immobilized Dendra2 in the original cell (Fig. 3C).

243 In addition, we found that this quantification method can be employed to evaluate the  
244 effects of ABA on the intercellular Dendra2 diffusivity. Within 1 hour after ABA treatment,  
245 intensity of the photoconverted Dendra2 became restricted in the original cell (Fig. 3, A and  
246 B). Notably, Dendra2 in ABA-treated protoplasts was also stable to proteolytic degradation  
247 (Supplemental Fig. S2). Consistently, by fitting the Dendra2 kinetics with the single  
248 exponential function, the  $\tau$  and  $B$  were smaller and larger in the ABA-treated sample,  
249 respectively as compared to the DMSO control (Fig. 3B). As the  $\tau$  represents how fast the  
250 Dendra2 intensity reaches the  $B$ , the  $\tau$  indicates how fast intercellular Dendra2 diffusivity is

251 suppressed in response to ABA and the  $B$  means the ratio of Dendra2 immobilized in the  
252 original cell as a result of ASD. Thus, our quantitative imaging analysis succeeded in  
253 characterizing the processes of intercellular diffusion of Dendra2 and its change in response to  
254 ABA.

255

### 256 **Quantitative dissection revealed PpSnRK2 and PpABI3 contributions to ASD**

257 Our phenotypic analyses indicated that *PpSnRK2A* and *PpABI3A* play more predominant  
258 roles than *PpABI1A* on ASD. We therefore next asked the question whether there is a  
259 differential contribution between *PpSnRK2A* and *PpABI3A* in regulating ASD. To this end, we  
260 measured the changes in the Dendra2 intensity over time in response to ABA in  
261 *ppsnrk2a/b/c/d* quadruple knockout (*ppsnrk2qko*) and *ppabi3a/b/c* triple knockout (*ppabi3tko*)  
262 mutants (*ProEF1 $\alpha$ :D2/ppsnrk2qko* and *ProEF1 $\alpha$ :D2/ppabi3tko*, respectively). We found that  
263 intercellular Dendra2 diffusion in the *ProEF1 $\alpha$ :D2/ppsnrk2qko* was observable irrespective of  
264 the presence and absence of ABA treatment (Fig. 4, A and B). The  $\tau$  and  $B$  obtained from the  
265 fittings were comparable between *ProEF1 $\alpha$ :D2* ( $\tau = 180$ ,  $B = 0.16$  in the median) and  
266 *ProEF1 $\alpha$ :D2/ppsnrk2qko* ( $\tau = 149$ ,  $B = 0.23$  in the median) in the absence of ABA or  
267 *ProEF1 $\alpha$ :D2/ppsnrk2qko* in the presence of ABA ( $\tau = 187$ ,  $B = 0.22$  in the median;  $P = 7.9 \times$   
268  $10^{-1}$  and  $P = 4.2 \times 10^{-1}$ ), respectively (Fig. 4, E and F). This indicates that PpSnRK2 is an  
269 indispensable factor for ASD.

270 On the other hand, although intercellular Dendra2 diffusion was observed in  
271 *ProEF1 $\alpha$ :D2/ppabi3tko* in the DMSO control (Fig. 4, C and D), the  $\tau$  in  
272 *ProEF1 $\alpha$ :D2/ppabi3tko* was calculated to be smaller than that in *ProEF1 $\alpha$ :D2* ( $\tau = 204$  and  
273  $266$  in the median), whereas the  $B$  was similar ( $B = 0.25$  and  $0.24$  in the median) (Fig. 4, G  
274 and H). This suggests that the intercellular Dendra2 diffusivity is higher in  
275 *ProEF1 $\alpha$ :D2/ppabi3tko* than in *ProEF1 $\alpha$ :D2* under the normal culture condition, possibly due  
276 to responsiveness to endogenous ABA. Upon ABA treatment, the observed ASD in  
277 *ProEF1 $\alpha$ :D2/ppabi3tko* was similar to that in *ProEF1 $\alpha$ :D2* (Fig. 3A and Fig. 4C). However,  
278 the  $\tau$  and  $B$  in *ProEF1 $\alpha$ :D2/ppabi3tko* was significantly higher and lower ( $\tau = 46$ ,  $B = 0.72$  in  
279 the median), respectively compared to that in the *ProEF1 $\alpha$ :D2* control ( $\tau = 10$ ,  $B = 0.82$  in the

280 median) (Fig. 4, G and H). Since the  $\tau$  indicates responsiveness to ABA to initiate ASD, the  
281 higher  $\tau$  in *ProEF1 $\alpha$ :D2/ppabi3tko* suggests that the disruption of *PpABI3* causes a temporal  
282 delay to initiate ASD. The lower  $B$  in *ProEF1 $\alpha$ :D2/ppabi3tko* can be also explained by this  
283 temporal delay before initiation of ASD. During the delay of ASD initiation, more Dendra2  
284 can diffuse from the original cells to neighboring cells in *ProEF1 $\alpha$ :D2/ppabi3tko* than  
285 *ProEF1 $\alpha$ :D2*. Thus, the Dendra2 intensity in the original cell decreased to a greater extent in  
286 *ProEF1 $\alpha$ :D2/ppabi3tko* than *ProEF1 $\alpha$ :D2* at the onset of ASD, which can result in the lower  
287  $B$  in *ProEF1 $\alpha$ :D2/ppabi3tko*.

288 Our results suggest that PpABI3 is responsible for the normal initiation of ASD. To gain  
289 better quantitative resolution on the temporal control of how PpABI3 facilitates this process,  
290 we introduced a time to the initiation of ASD ( $A$ ) in this study (Fig. 4I). Because complete  
291 suppression of the Dendra2 diffusion between cells requires infinite time due to the exponential  
292 indeterminate form (see Materials and Methods), we here considered the duration required for  
293 the Dendra2 intensity to the 90% of the steady state level ( $A_{90}$ ). The  $A_{90}$  allows us to compare  
294 the temporal difference to initiate ASD in the absence and presence of *PpABI3*. We  
295 determined that in *ProEF1 $\alpha$ :D2* the  $A_{90}$  is 24 min, whereas in *ProEF1 $\alpha$ :D2/ppabi3tko* the  $A_{90}$   
296 is increased to 105 min. This indicates an 81-min delay to arrest the Dendra2 diffusion in  
297 response to ABA in *ProEF1 $\alpha$ :D2/ppabi3tko*. We obtained a similar temporal delay in the  
298 *ProEF1 $\alpha$ :D2/ppabi3tko* when  $A_{85}$  and  $A_{95}$  were used, further confirming the robustness of our  
299 interpretation.

300

### 301 **Suppression of intercellular Dendra2 diffusion by PpABI3 is callose-independent**

302 Using TEM approach, we previously reported that the PD aperture size was reduced by 9-nm  
303 after ABA treatment. Aniline blue staining also showed that there are little changes in the  
304 callose deposition on cross walls (Kitagawa et al., 2019). However, it is still unclear whether  
305 conventional aniline blue staining in fixed cells is sufficient to support the  
306 callose-independent regulation of ASD. We therefore improved the aniline blue staining  
307 method and established its live-imaging method to observe changes in callose deposition on  
308 cross walls between targeted cells after ABA treatment. Callose accumulation at the cross wall

309 was detectable during cell divisions in living protonemal cells even in the presence of aniline  
310 blue solution (Supplemental Fig. S4A). Moreover, we were able to observe intercellular  
311 Dendra2 diffusion and ASD in this method (Supplemental Fig. S4B), indicating that link  
312 between intercellular Dendra2 diffusivity and the extent of callose deposition on cross walls is  
313 evaluable. We analyzed changes of callose deposition in the *ProEF1α:D2* on the same cross  
314 wall between the 11th and 12th cell for 180 min after ABA treatment, and found that callose  
315 signal intensity was constant throughout the observation, irrespective of ABA treatment. (Fig.  
316 5, A and D). Intriguingly, callose intensity was also unchanged in the *ProEF1α:D2/ppabi3tko*  
317 as well as the *ProEF1α:D2/ppsnrk2qko* (Fig. 5, B-D). To investigate the callose deposition on  
318 cross walls between the 11th and 12th cell in greater details, we acquired images with better  
319 resolution from control and ABA-treated samples, at 20-, 100- and 180-min time points.  
320 When observed at 0.3- $\mu$ m optical slice, we detected punctate signals on cross walls (Fig. 5,  
321 E-G; Supplemental Fig. S5, A and B), which resembles the PD-associated callose  
322 accumulation as detected previously by callose immunostaining (Kitagawa et al., 2019).  
323 There was no significant increase in the density of punctate signals between the control and  
324 ABA-treated samples in *ProEF1α:D2*, *ProEF1α:D2/ppsnrk2qko*, and *ProEF1α:D2/ppabi3tko*  
325 (Fig. 5H), and also *PpABI3AiOX/ProEF1α:D2* (Supplemental Fig. S5C). Our results suggest  
326 that PpABI3 does not increase the density of PD-associated callose in response to endogenous  
327 and exogenous ABA. Collectively, our data further supported that PpSnRK2 and PpABI3  
328 facilitates ASD in a callose-independent manner.

329

### 330 **PpABI3 is required in salt stress tolerance acquisition of protonemal cells in response to** 331 **ABA**

332 Given that PpABI3 facilitates the initiation of ASD in protonemal cells, we wonder whether  
333 this observation is related to any physiological response(s). One possible response is  
334 acquisition of salt stress tolerance since ABA plays crucial roles on this process (Takezawa et  
335 al., 2015). To test this hypothesis, we set out to determine the protonemal viability rate after  
336 salt stress treatment by counting propidium iodide (PI)-stained dead cells (Fig. 6A). In the  
337 control, all cells in *ProEF1α:D2*, *ppsnrk2qko/ProEF1α:D2*, and *ppabi3tko/ProEF1α:D2* were

338 alive (viability:  $100 \pm 0$  %) (Fig. 6B). In *ProEF1 $\alpha$ :D2*, the cell viability under salt stress  
339 without and after 5-, 20-, and 100-min ABA pretreatment was  $51 \pm 33\%$ ,  $47 \pm 41\%$ ,  $83 \pm 9\%$ ,  
340 and  $87 \pm 12\%$ , respectively (Fig. 6B), indicating that salt stress tolerance was significantly  
341 induced after 20-min ABA pretreatment. In *ppsnrk2qko/ProEF1 $\alpha$ :D2*, cell viability under salt  
342 stress without and after 5-, 20-, and 100-min ABA pretreatment was  $13 \pm 26\%$ ,  $9 \pm 19\%$ ,  $5 \pm$   
343  $9\%$ , and  $14 \pm 26\%$  (Fig. 6B). This result showed that *ppsnrk2qko/ProEF1 $\alpha$ :D2* is  
344 ABA-insensitive during acquisition of salt stress tolerance and is consistent with the essential  
345 role of PpSnRK2 in ASD (Fig. 4, A, B, E and F). On the contrary, cell viability in  
346 *ProEF1 $\alpha$ :D2/ppabi3tko* under salt stress without and after 5-, 20-, and 100-min ABA  
347 pretreatment was  $43 \pm 26\%$ ,  $35 \pm 37\%$ ,  $54 \pm 27\%$  and  $76 \pm 18$  % (Fig. 6B), indicating that salt  
348 stress tolerance was significantly induced after 100-min ABA treatment. There was about  
349 80-min delay in acquisition of salt stress tolerance in *ProEF1 $\alpha$ :D2/ppabi3tko* when compared  
350 to *ProEF1 $\alpha$ :D2*. These results indicate that the PpABI3-mediated ABA signaling contributes  
351 to the acquisition of salt stress tolerance in around 80 min, which is quite similar to the value  
352 observed in PpABI3-mediated ASD response (Fig. 4I). This suggests a plausible mechanism  
353 connecting the regulation of PD permeability and viability against salt stress tolerance by  
354 PpABI3.

355

356

## 357 **Discussion**

358 This study provides quantitative dissection on the contributions of ABA signaling components  
359 in regulating protonemal PD permeability. Our analysis revealed that, in contrast to the  
360 essential roles of PpSnRK2 in ASD, PpABI3 plays a specific role in promoting the initiation  
361 of ASD within 80 min. We further unraveled that PpABI3 is required for the rapid acquisition  
362 of salt stress tolerance in protonemal cells, thereby contributing to the survival strategy during  
363 abiotic stress conditions. Interestingly, these two processes that mediated by PpABI3 occur in  
364 a similar timescale of tens of minutes, suggesting the promotive role of PpABI3 in  
365 coordinating PD permeability and stress tolerance through the ABA signaling.

366

### 367 **Regulatory mechanism of ASD in protonemal cells of *P. patens***

368 Although our previous study reported the phenomenon of ASD and the contribution of  
369 endogenous ABA in ASD (Kitagawa et al., 2019), it remains elusive which of the ABA  
370 signaling components and how they are involved in this process. Here, we provide evidence  
371 to show that PpSnRK2 and PpABI3 are essential and promotive factors in the ABA signaling  
372 to drive ASD in protonemal cells. Our quantitative analysis based on the newly introduced *A<sub>90</sub>*  
373 further revealed that ASD is almost initiated within this time frame after ABA treatment.  
374 Since PpSnRK2 is essential for ASD and is involved in the phosphorylation of ABA signaling,  
375 PpSnRK2 seems to phosphorylate ASD-related factors within 24 min based on *A<sub>90</sub>* in  
376 *ProEF1α:D2*. Previously a phosphoproteomic analysis of the ABA signaling pathway  
377 identified 74 phosphopeptides (51 phosphorylated proteins except for PpSnRK2s) within 15  
378 min after ABA treatment (Amagai et al., 2018). We speculate that the downstream targets of  
379 PpSnRK2 to trigger ASD are present in this phosphoprotein list. In consistent with this, seven  
380 of these phosphoproteins are orthologues found in the proteome of *A. thaliana* PD  
381 (Fernandez-Calvino et al., 2011; Amagai et al., 2018). However, their functions in regulating  
382 PD permeability and localizations around PD have not yet been demonstrated. It would be  
383 worth examining the contribution of their phosphomimic forms on ASD to uncover molecular  
384 mechanism of the ABA signaling in ASD.

385 In contrast to these downstream targets of the PpSnRK2, PpABI3 is not phosphorylated  
386 in the ABA signaling (Nakashima et al., 2009; Umezawa et al., 2013; Wang et al., 2013;  
387 Amagai et al., 2018). ABA INSENSITIVE 5 (ABI5) of *P. patens* is instead phosphorylated  
388 within 15 min after ABA treatment (Amagai et al., 2018). PpABI3A is known to interact with  
389 barley ABI5, which enhances transactivation of an ABA-responsive wheat Em promoter  
390 without ABA treatment (Marella et al., 2006). Therefore, one possible regulatory mechanism  
391 in ASD may be the co-regulation by a PpABI3 and PpABI5 heterodimer which accelerates the  
392 ASD downstream of PpSnRK2. If this is the case, the PpABI3-mediated ASD should involve  
393 transcriptional regulation since PpABI3 is a known transcriptional factor. Because basal  
394 expression of *PpABI3* is required for the protonemal growth in *P. patens* (Zhao et al., 2018),  
395 this weak but constitutive expression of *PpABI3* may also contribute to promote the rapid

396 initiation of ASD. This hypothesis is consistent with our observation that intercellular  
397 Dendra2 diffusion in the *ProEF1α:D2/ppabi3tko* is slightly higher than *ProEF1α:D2* under  
398 normal culture conditions. In addition, *de novo* synthesized PpABI3 in response to ABA may  
399 further augment the ABA signaling to boost ASD.

400 A key question relevant to the PpABI3-mediated regulation of ASD would be, what is  
401 the downstream mechanism? A previously reported proteome analysis study identified  
402 SYNAPTOTAGMIN (SYT) as a candidate target of PpABI3-mediated ABA signaling (Yotsui  
403 et al., 2016). SYT is annotated as a C2 domain containing protein. In *A. thaliana*, AtSYTA  
404 was shown to be a PD-localized protein (Schapire et al., 2008; Fernandez-Calvino et al., 2011;  
405 Levy et al., 2015; Perez-Sancho et al., 2015). It is tempting to hypothesize that PpSYT may  
406 tether plasma membrane and endoplasmic reticulum to restrict PD permeability as shown in  
407 other multiple C2 domains and transmembrane region proteins (Brault et al., 2019).  
408 Importantly, this regulation by the SYT may occur in a callose-independent manner, which is  
409 consistent with observation that the PpABI3-mediated ASD did not involve any callose  
410 deposition around PD.

411 Among the ABA signaling components, contribution of PpABI1 on ASD was less  
412 prominent compared to that of PpSnRK2 and PpABI3. In contrast to our finding,  
413 ABI1-mediated ABA signaling in *Populus* is involved in the regulation of PD permeability in  
414 bud dormancy (Tylewicz et al., 2018). This discrepancy can be explained by an interaction  
415 between ABI1 and SnRK2 and/or emergence of PDLP which can modify the ABA sensitivity  
416 in *Populus* (Komatsu et al., 2013; Lee, 2014; Brunkard and Zambryski, 2017). Our data  
417 warrant further investigations to unravel the molecular mechanisms of PpSnRK2-, PpABI3-,  
418 and PpABI1-mediated ABA signaling in ASD. This would be helpful to extend our  
419 understanding on how PD permeability is regulated in response to abiotic stresses.

420

### 421 **Cellular physiological responses associated with ABA signaling in ASD**

422 We previously established a simple simulation model for PD permeability based on a  
423 relationship between PD aperture and molecule size (Kawade and Tanimoto, 2015; Kawade et  
424 al., 2017). Although this model is well recapitulated in *in vivo* experiments using GFP



425 diffusivity through PD under the normal condition, it failed to explain the connection between  
426 ASD occurrence and the reduction in PD aperture size. Although upon ABA treatment the PD  
427 aperture was reduced from 38 nm to 29 nm (Kitagawa et al., 2019), the Dendra2 molecules  
428 with a Stokes radius of Dendra2 (2.4 nm) should still be able to diffuse through the tightened  
429 PD aperture without much difficulty (Sadovsky et al., 2017). However this is not the case as  
430 ABA treatment inhibits the intercellular ABA diffusion. These observations suggest that  
431 additional elements independent of PD structural modification such as cytoplasmic viscosity  
432 can be involved in ASD. Indeed, in response to ABA and some environmental stresses, sugar  
433 and sugar alcohol has been reported to accumulate in *P. patens* protonemal cells as compatible  
434 solutes (Nagao et al., 2005; Nagao et al., 2006; Oldenhof et al., 2006; Komatsu et al., 2013;  
435 Arif et al., 2018). This increment in the compatible solutes can enhance cytoplasmic viscosity  
436 (Wolkers et al., 1998; Golovina et al., 2001) which can affect macromolecular diffusivity  
437 (Verkman, 2002).

438 Lastly we pursued cellular physiological responses regulated by PpABI3 in protonemal  
439 tissues and found that salt stress tolerance is conferred by the PpABI3 in a time frame similar  
440 to that of ASD. A series of studies had been carried out to investigate mechanisms involved to  
441 acquire various stress tolerance against desiccation, hyperosmolality, low temperature, and  
442 freezing in an order of 24 hours after ABA treatment (Minami et al., 2005; Komatsu et al.,  
443 2009; Khandelwal et al., 2010; Komatsu et al., 2013; Saruhashi et al., 2015; Tan et al., 2017).  
444 Involvement of PpABI3-mediated transcriptional regulation in these processes has also been  
445 reported (Khandelwal et al., 2010; Tan et al., 2017). However, our results showed that the  
446 acquisition of salt stress tolerance mediated by PpABI3 was much more rapid and occurred  
447 within 20 min of ABA pretreatment. Disruption of *PpABI3* compromised this rapid induction  
448 of salt stress tolerance and resulted in an approximately 80-min delay for the tolerance  
449 acquisition. Our studies, together with these results, indicate that PpABI3 plays roles in  
450 acquiring stress tolerance both in short and long time frame. We speculate that basal  
451 expression of the PpABI3 contributes to short term environmental stresses tolerance, and this  
452 “pre-existing” PpABI3 in combination with *de novo* synthesized PpABI3 are involved in the  
453 regulation of a transcriptional network to induce more robust and persisting stress tolerances.

454 Autoregulation of the ABI3 transcription may accelerate the downstream reaction until  
455 endogenous ABA is gradually synthesized (Minami et al., 2005; Bedi and Chaudhuri, 2018).  
456 Thus at the moment, it is tempting to speculate that whether and how PpABI3-mediated ASD  
457 and acquisition of salt stress tolerance are mechanistically and functionally coordinated in a  
458 relatively short duration. Nevertheless, it is also possible that the decreased viability in  
459 *ProEF1α:D2/ppsnrk2ako* or *ProEF1α:D2/ppabi3tko* is attributed to the repression of  
460 PpSnRK2- and/or PpABI3-mediated regulation of salt stress tolerance, which is independent  
461 of the regulation of cell-to-cell communication. Future experiments to address this point  
462 should provide further understanding of the relationship between cell-to-cell communication  
463 and physiological response at a cellular level.

464

465

## 466 **Materials and Methods**

### 467 **Plant materials and growth conditions**

468 The *Physcomitrella patens* WT strain used in this study was Gransden 2004 (Rensing et al.,  
469 2008). The *ProEF1α:D2*, *ppsnrk2qko*, and *ppabi3tko* lines were described previously  
470 (Khandelwal et al., 2010; Kitagawa and Fujita, 2013; Shinozawa et al., 2019). The plants  
471 were cultured on BCDAT medium with 0.8% (w/v) agar under continuous white light at 25°C  
472 for three to five days (Nishiyama et al., 2000).

473

### 474 **Vector constructions**

475 We obtained the full-length cDNA clone of *pphn8m2* including *PpABI1A* from the RIKEN  
476 BioResource Center (Resource number: pdp31463). A synonymous mutation in the open  
477 reading frame (ORF) of *PpABI1A* (*PpABI1A<sup>G1610A</sup>*) in pdp31463 was corrected with the  
478 primer set of 5'-ATGAGGCGGTCTGCGATATTG-3' (Forward) and  
479 5'-CTATCTATCCCTGGGAACCTTTTAAGTC-3' (Reverse). The resulting fragment was used  
480 to amplify the ORF of *PpABI1A* with the primer set of  
481 5'-CACCATGGCCACAGCTAAACTTGTAGAAG-3' (Forward) and  
482 5'-CTATCTATCCCTGGGAACCTTTTAAGTC-3' (Reverse). The ORF fragment of *PpABI1A*

483 was cloned into the pENTR/D-TOPO vector (Thermo Fisher Scientific) and confirmed by  
484 sequencing. To introduce a mutation mimicking *abil-1* of *A. thaliana* (Koornneef et al.,  
485 1984) in the ORF fragment of *PpABI1A* (*PpABI1A*<sup>G333D</sup>), PCR was performed with the primer  
486 set of 5'-ATGGGCATGATGGATCGC-3' (Forward) and  
487 5'-CGTATACTCCAAAATAATGTAAAGGAGC-3' (Reverse) using the pENTR/D-TOPO  
488 vector containing *PpABI1A* as the template, and then the resultant fragment was ligated with  
489 DNA ligation kit (TaKaRa). The resultant plasmid was subjected to LR reaction with the  
490 destination pPOG1 vector using LR clonase II plus enzyme mix (Thermo Fisher Scientific)  
491 (pPOG1-*PpABI1A*<sup>G333D</sup>).

492 The ORF fragment of *PpSnRK2A* from pGAD424 vector containing *PpSnRK2A* was  
493 amplified with the primer set of 5'-CACCATGGATATTCCGAGCATGCATGACCAC-3'  
494 (Forward) and 5'-CATTGCGCACACAAACTCCCCAC-3' (Reverse). The ORF fragment of  
495 *PpSnRK2A* was cloned into the pENTR/D-TOPO vector (Thermo Fisher Scientific) and  
496 confirmed by sequencing. The resultant plasmid was subjected to LR reaction with the  
497 destination pPGX8 (Kubo et al., 2013) vector using LR clonase II plus enzyme mix (Thermo  
498 Fisher Scientific) (pPGX8-*PpSnRK2A*).

499 We obtained the full-length cDNA clones of *pphn37a15* including *PpABI3A* from the  
500 RIKEN BioResource Center (Resource number: pdp41729). The ORF fragment of *PpABI3A*  
501 in pdp41729 was amplified with the primer set of  
502 5'-CACCATGGTGCTCCTATCGAGTGTG-3' (Forward) and  
503 5'-TCCTGCGGGCTCGGTC-3' (Reverse). The ORF fragment of *PpABI3A* was cloned into  
504 the pENTR/D-TOPO vector (Thermo Fisher Scientific) and confirmed by sequencing. The  
505 resultant plasmid was subjected to LR reaction with the destination pPGX8 (Kubo et al.,  
506 2013) vector using LR clonase II plus enzyme mix (Thermo Fisher Scientific)  
507 (pPGX8-*PpABI3A*).

508 The pPOG1-*PpABI1A*<sup>G333D</sup>, pPGX8-*PpSnRK2A*, and pPGX8-*PpABI3A* were digested  
509 with the restriction enzyme *Sse8387I* (TaKaRa) before transformation.

510

511 **Transgenic lines**

512 Transformation was performed based on the polyethylene glycol-mediated method  
513 (Nishiyama et al., 2000).

514 The *PpABI1A*<sup>G333D</sup>*OX/ProEF1α:D2* lines were generated by introducing the  
515 *Sse8387I*-digested pPOG1-*PpABI1A*<sup>G333D</sup> fragments into the *ProEF1α:D2* genetic  
516 background. Stable transformants were selected on BCDAT agar medium containing 30 mg/L  
517 hygromycin B (Wako) twice. The expression of *PpABI1A*<sup>G333D</sup> in  
518 *PpABI1A*<sup>G333D</sup>*OX/ProEF1α:D2* lines was confirmed through RT-PCR with the primer set of  
519 5'-TGTGGTGCCTAGTGACGCTG-3' (Forward) and 5'-ATTCGCTGCCTGCGATCCAT-3'  
520 (Reverse) for *PpABI1A*<sup>G333D</sup> and the primer set of 5'-TGCCATTAAGACGGCTATCA-3'  
521 (Forward) and 5'-CGAGATTATTTCCAACAGATGGTCTA-3' (Reverse) for *PpGAPDH* (as  
522 an internal control) (Supplemental Fig. S6).

523 *PpSnRK2AiOX/ProEF1α:D2* lines were generated by introducing the *Sse8387I*-digested  
524 pPGX8-*PpSnRK2A* fragments into the *ProEF1α:D2* genetic background. Stable  
525 transformants were selected on BCDAT agar medium containing 30 mg/L hygromycin B  
526 (Wako) twice. The gene targeting was verified by genomic PCR with the primer set of  
527 5'-ACAAGTTTGTACAAAAAAGCAGGCT-3' (Forward) and  
528 5'-CATTGCGCACACAAACTCCC-3' (Reverse) which bind the outside from the 5'-end of  
529 ORF and the 3'-end of ORF of *PpSnRK2A*, and the primer set of  
530 5'-CGCTTAGGCAGGAGGCCGTT-3' (Forward) and  
531 5'-CACCTCTGGCCCGTGACAA-3' (Reverse) which bind the inside of transgene and the  
532 outside of the 3'-end of the *P. patens* inter-genic 1 (PIG1) site.

533 *PpABI3AiOX/ProEF1α:D2* lines were generated by introducing *Sse8387I*-digested  
534 pPGX8-*PpABI3A* fragments into the *ProEF1α:D2* genetic background. Stable transformants  
535 were selected on BCDAT agar medium containing 30 mg/L hygromycin B (Wako) twice. The  
536 gene targeting was verified by genomic PCR with the primer set  
537 5'-ACAAGTTTGTACAAAAAAGCAGGCT-3' (Forward) and  
538 5'-TCCTGCGGGCTCGGTCTTCA-3' (Reverse) which bind the outside from the 5'-end of  
539 ORF and the 3'-end of ORF of *PpABI3A*, and with the primer set  
540 5'-CGCTTAGGCAGGAGGCCGTT-3' (Forward) and

541 5'-CACCCCTCTGGCCCGTGACAA-3' (Reverse) which bind the PIG1 site.

542 The *ProEF1α:D2/ppsnrk2qko* and *ProEF1α:D2/ppabi3tko* lines were established by  
543 introducing the *ProEF1α:D2* construct (pT1OG-Dendra2) (Kitagawa and Fujita, 2013) into  
544 the *ppsnrk2qko* and *ppabi3tko* genetic backgrounds, respectively (Khandelwal et al., 2010;  
545 Shinozawa et al., 2019). Stable transformants were selected on BCDAT agar medium  
546 containing 100 mg/L zeocin (Invitrogen) twice.

547 The independently generated transgenic lines underwent the following quantitative  
548 RT-PCR, microscopy and photoconversion assay, callose staining with aniline blue, and  
549 viability test against salt stress, in which we confirmed reproducibility.

550

### 551 **Quantitative RT-PCR**

552 Protonemal tissues of *ProEF1α:D2*, *PpSnRK2AiOX/ProEF1α:D2*, and  
553 *PpABI3AiOX/ProEF1α:D2* lines were cultured for 10 days under red light on BCDAT agar  
554 medium overlaid with cellophane sheets. The cellophane with the 10-day-old culture of  
555 *ProEF1α:D2* were then transferred onto BCDAT agar medium with 50 μM ABA, and  
556 subjected to additional culture for 1, 6, or 12 hours to investigate the expression levels of  
557 *PpSnRK2A-D* (Pp3c5\_21160V3, Pp3c6\_16600V3, Pp3c6\_11090V3 and Pp3c5\_17150V3,  
558 respectively) and *PpABI3A-C* (Pp3c2\_3370V3, Pp3c17\_16470V3 and Pp3c4\_7320V3,  
559 respectively) in response to ABA. In the negative control, the cellophanes with the 10-day-old  
560 culture of *ProEF1α:D2* were directly used to investigate the expression level of *PpSnRK2A-D*  
561 and *PpABI3A-C* without additional culture on BCDAT agar medium with 50 μM ABA. For  
562 inducible experiments, the cellophanes with the 10-day-old cultures of *ProEF1α:D2*,  
563 *PpSnRK2AiOX/ProEF1α:D2*, and *PpABI3AiOX/ProEF1α:D2* lines on BCDAT agar medium  
564 were transferred onto BCDAT agar medium with 1 μM β-estradiol (or 0.1% (v/v) DMSO as  
565 the negative control). The plant tissues were used for RT-PCR analysis 24 hours after transfer  
566 to confirm the inducible overexpression of *PpSnRK2A* or *PpABI3A*.

567 Total RNA was purified from the protonemal tissues with RNeasy Plant Mini Kit  
568 (QIAGEN). First-strand cDNA was synthesized with ReverTra Ace qPCR RT Master Mix  
569 with gDNA Remover (TOYOBO) according to the manufacture's instruction. qRT-PCR was

570 performed using an ABI 7500 RealTimePCR System (Applied Biosystems) with the  
571 THUNDERBIRD qPCR mix (TOYOBO). The data were analyzed by the  $\Delta\Delta C_t$  method for  
572 relative quantification of the transcript levels. The transcript levels were normalized against  
573 riboflavin kinase gene (*RFK*) (Pp3c12\_7730V3) or 3-hydroxyisobutyryl-CoA hydrolase gene  
574 (*HIBCH*) (Pp3c4\_17830V3), whose expression levels were reported to be robust against ABA  
575 treatment (Khraiwesh et al., 2015). The data were collected from three independent biological  
576 replicates with technical triplicates, and subjected to the statistical analysis of Welch's *t*-test.  
577 The used primers in the qRT-PCR is listed in Supplemental Table S1.

578

### 579 **Microscopy and photoconversion assay**

580 Three- to five-day-old protonemal tissues were inoculated into 500  $\mu$ L of BCDAT medium  
581 containing 0.5% glucose (BCDATG) solidified with 0.5% gellan gum in 4-well chamber  
582 slides (no. 5222-004; Iwaki), and then covered with the additional 250  $\mu$ L of the medium. To  
583 suppress branching of the protonemata, the samples were cultured under continuous red light  
584 for 10 days as previously reported (Kitagawa and Fujita, 2013) except for  
585 *ProEF1 $\alpha$ :D2/ppsnrk2qko* (for 15 days) due to its slower growth under red light. *ProEF1 $\alpha$ :D2*  
586 was also cultured for 15 days when compared with *ProEF1 $\alpha$ :D2/ppsnrk2qko*. In the test of  
587 ABA effects, 50 mM ABA or DMSO was added into wells of the 4-well chamber slides just  
588 after photoconversion to final concentrations of 50  $\mu$ M and 0.1% (v/v), respectively. In the  
589 test of overexpression effect of *PpSnRK2A* or *PpABI3A*, 1 mM  $\beta$ -estradiol or DMSO was  
590 added into wells of the 4-well chamber slides 24 hours before photoconversion to final  
591 concentrations of 1  $\mu$ M and 0.1% (v/v), respectively. For assessment of protonemal growth  
592 and morphology, the samples were observed under a microscope (DM 2500, Leica).

593 Photoconversion of Dendra2 was carried out using a confocal laser-scanning microscope  
594 (Nikon A1, Nikon) in the 12th cells from the apices in protonemata with 405-nm diode laser  
595 (10.0% laser output, 36 mW) with 3 iterations (8 sec/frame, zoom 4 $\times$ ) using the PlanApo  
596 10x/0.45 NA objective. Time-lapse imaging was subsequently performed with the objective  
597 lens PlanApo 10x /0.45 NA and 561-nm solid laser (2.0% laser output, 10 mW) at 20-min  
598 intervals for 720 min. Five z-stack images of size 1024  $\times$  1024 pixels were acquired at 6- $\mu$ m

599 steps in each interval. The pinhole size was set to 16.60  $\mu\text{m}$  in diameter, which yields a 7.29  
600  $\mu\text{m}$  optical slice in this condition.

601 We manually measured the mean fluorescence intensity of photoconverted Dendra2 in  
602 the whole regions of the laser-irradiated cells or the neighboring cells, and subtracted the  
603 mean fluorescence intensity of the surrounding medium region at each time point with Fiji  
604 software (ImageJ; <https://imagej.net/Fiji>). Based on the previous analysis (Kawade et al.,  
605 2017), the kinetics of Dendra2 intensity from 0 to 720 min after photoconversion was fitted  
606 by an exponential function as

$$607 \quad I(t) = (I_0 - B)e^{-t/\tau} + B, \quad (1)$$

608 where  $I(t)$  and  $I_0$  are fluorescence intensity of Dendra2 at a time  $t$  and just after  
609 photoconversion, respectively, normalized with the mean fluorescence intensity per pixel just  
610 after photoconversion ( $I_0 = 1$ );  $\tau$  is a time constant of Dendra2 diffusivity or responsiveness to  
611 ABA treatment for ASD;  $B$  is an immobile fraction of Dendra2 in the original cell.  $\tau$  and  $B$  are  
612 free parameters determined by minimizing the residual sum of squares (RSS) between the  
613 measured data and the fitting function (1) by using custom MATLAB scripts.

614 Dendra2 intensity decreased over time and reached the level at the steady state in our  
615 experiment. To evaluate how this profile is affected in response to ABA during the  
616 progression to ASD, we here calculated a decrease ratio of Dendra2 intensity ( $x\%$ ) at an  
617 arbitrary point of time  $t$  against the Dendra2 intensity at the steady state. The decrease ratio of  
618 Dendra2 intensity at a time  $t$  is described as follows:

$$619 \quad (I(t) - B)/(I_0 - B) = 1 - x/100. \quad (2)$$

620 When solving for  $I(t)$ , we obtained the following equation:

$$621 \quad I(t) = (1 - x/100) \times (I_0 - B) + B. \quad (3)$$

622 By solving for  $x$  after introduction of (3) into (1), the decreased ratio of Dendra2  
623 intensity  $x$  was summarized by using  $t$  and  $\tau$ , given as:

$$624 \quad x = 100 \times (1 - e^{-t/\tau}). \quad (4)$$

625 Because, in this case,  $t$  represents time required for reaching the Dendra2 intensity to the  
626  $x\%$  of the steady state level, we introduced a new parameter  $Ax$  for this specific time instead  
627 of  $t$  to avoid confusion as follows:

628 
$$x = 100 \times (1 - e^{(-Ax/\tau)}).$$
 (5)

629 By using this equation, we were able to evaluate how rapidly ASD is observed in  
630 response to ABA.  $A_{90}$  nearly equals to 2.3-fold value of  $\tau$ .

631

### 632 **Assessment of Dendra2 degradation in protoplasts**

633 Protoplasts were obtained from three- to five-day-old protonemal tissues of *ProEF1a:D2*  
634 through 20-min treatment of 2% (w/v) Driserase dissolved in 8% (w/v) mannitol (Kyowa  
635 Hakko Kogyo Co., Ltd.) solution with gentle mix at 5-min intervals. The protoplasts were  
636 filtered through a mesh (CellTrics ®, 50  $\mu\text{m}$ , Partec) into a 12 mL tube, collected by  
637 centrifugation at 1,000 rpm, and suspended in 8% (w/v) mannitol solution. After  
638 centrifugation again, the protoplasts were suspended in 250  $\mu\text{L}$  of BCDATG medium  
639 containing 0.5% (w/v) gellan gum and 6% (w/v) mannitol, and put into each well of 8-well  
640 chamber slides (no. 5232-008; Iwaki), and then covered with additional 500  $\mu\text{L}$  of BCDATG  
641 medium containing 0.5% (w/v) gellan gum and 6% (w/v) mannitol .

642 Images of protoplasts were obtained just after and 12 hours after photoconversion. Mean  
643 fluorescence intensity per pixel of photoconverted Dendra2 in the protoplasts was analyzed  
644 with Fiji software (ImageJ; <https://imagej.net/Fiji>). Dendra2 degradation was assessed with  
645 the ratio of mean fluorescence intensity just after photoconversion and at 12 hours after  
646 photoconversion. MG-132 (final concentration 50  $\mu\text{M}$ ) was added into the wells of 8-well  
647 chamber slides 1.5 hours before photoconversion of Dendra2 for the negative control of  
648 proteolytic degradation.

649

### 650 **Callose staining with aniline blue**

651 Aniline blue (Wako) was dissolved in 100 mM phosphate buffer (pH 8.7) to a concentration  
652 of 5.0% (w/v), and sterilized by filtration (pore size = 0.22  $\mu\text{m}$ ). The 5.0% (w/v) aniline blue  
653 solution was further dissolved in the buffer to a concentration of 1.6% (w/v). The color of  
654 aniline blue solution was changed from blue to brownish yellow when incubated more than 2  
655 days at room temperature and exposure to air at several times. Staining was carried out after  
656 the color change. We found that the color aniline blue solution changed into yellow-brown



657 when dissolving in the pH 8.7 phosphate buffer. This is similar to the case of dissolving  
658 aniline blue in  $K_3PO_4$  (pH 12) solution as the previous reported (Zavaliev and Epel, 2015).

659 The aniline blue solution was added to samples to a concentration of 0.1% (w/v) one day  
660 before observation under Nikon A1 confocal microscope (Nikon). To detect change in callose  
661 signal with aniline blue, time-lapse imaging was performed with the PlanApo-VC 20x/0.75  
662 NA objective (zoom 4×) and 405-nm diode laser (2.0% laser output, 36 mW) at 20-min  
663 intervals for 180 min. Five z-stack images of size  $1024 \times 1024$  pixels were acquired at 3  
664  $\mu$ m-steps in each interval. The pinhole size was set to 14.05  $\mu$ m in diameter, which yields a  
665 1.77  $\mu$ m optical slice in this condition. To calculate the density of punctate signals from  
666 callose, images were acquired with the PlanApo-VC 100xH/1.4 NA objective (zoom 4×) and  
667 405-nm diode laser (100% laser output, 36 mW). The pinhole size was set to 40.87  $\mu$ m in  
668 diameter, which yields a 0.31  $\mu$ m optical slice in this condition. We calculate the density of  
669 punctate signals from the obtained images with manual adjustments of brightness and contrast.  
670 For counting the punctate signals, we manually adjust contrast and/or brightness so that we  
671 can distinguish each punctate signal in the same image possessing different signal intensity of  
672 the cross wall.

673

#### 674 **Viability test against salt stress**

675 Three- to five-day-old protonemal tissues were inoculated into 200  $\mu$ L of BCDATG with  
676 0.5% gellan gum, in glass-based dishes with 27-mm-diameter chambers (no. 3960-035;  
677 Iwaki) and then covered with additional 300  $\mu$ l of the medium. In addition, 8.5 mL of liquid  
678 BCDATG medium was poured on the culture medium to avoid drying. The samples were  
679 cultured for 10 days under continuous light with the glass side up.

680 The liquid medium was exchanged with 8.5 mL of liquid BCDATG medium containing  
681 ABA to final concentration 50  $\mu$ M. The samples were incubated for 20 and 100 min. These  
682 steps were skipped in the case without ABA treatment. To give salt stress to protonemal  
683 tissues, the liquid medium was exchanged with 8.5 mL of liquid BCDATG medium  
684 containing NaCl to a final concentration of 600 mM for 60 min. To assess cell viability, the  
685 liquid medium containing NaCl in the samples were exchanged with 3 mL of 50  $\mu$ g/mL

686 propidium iodide (PI) and incubated for 5 min, and then washed out with 8.5 mL of liquid  
687 BCDATG medium for 5 min. In the control, the samples were directly subjected to the PI  
688 staining without salt stress treatment.

689 Under a stereomicroscope (M165 FC, Leica), we counted the number of dead cells  
690 among 14 cells from the apices in each protonema as judged with the PI signal in nuclei.

691

692

### 693 **Supplementary data**

694 **Supplemental Figure S1.** Expression level of *PpSnRK2* and *PpABI3* in protonemal tissues.

695 **Supplemental Figure S2.** Measurement of the Dendra2 degradation rate.

696 **Supplemental Figure S3.** Change in fluorescence intensity of Dendra2 in the neighboring  
697 cells of the photoconverted cells.

698 **Supplemental Figure S4.** Callose signal on newly formed cross walls and intercellular Den-  
699 dra2 diffusivity under the condition of callose staining with aniline blue.

700 **Supplemental Figure S5.** Live-cell imaging of callose staining in  
701 *PpABI3AiOX/ProEF1α:D2*.

702 **Supplemental Figure S6.** Expression of *PpABIIA<sup>G333D</sup>* in protonemal tissue of  
703 *PpABIIA<sup>G333D</sup>OX/ProEF1α:D2*.

704 **Supplemental Table S1.** Primer sequences in qPCR.

705

706

### 707 **Acknowledgements**

708 We are grateful to O.K. Teh. (Hokkaido University) for correcting this manuscript. We thank  
709 Y. Hiwatashi (Miyagi University) and M. Hasebe (National Institute for Basic Biology) for  
710 the pPGX8 and pPOG1 vectors. RIKEN BioResource Center for the pdp31463 and pdp41729  
711 plasmids; the Spectrography and Bioimaging Facility and the Functional Genomics Facility  
712 (NIBB Core Research Facilities), and the Model Plant Research Facility (NIBB BioResource  
713 Center) for technical supports.

714

715

716 **Figure legends**

717 **Figure 1. Morphology and growth of protonemal cells in transgenic lines overexpressing**  
718 ***PpABI1A*<sup>G333D</sup>, *PpSnRK2A*, or *PpABI3A*.**

719 A and B, Representative images of protonemal cells at apical and basal positions after DMSO  
720 or ABA treatment in *ProEF1α:D2* (A) and *PpABI1A*<sup>G333D</sup>*OX/ProEF1α:D2* (B). C to E,  
721 Representative images of protonemal cells at apical and basal positions after DMSO or  
722 β-estradiol treatment in *ProEF1α:D2* (C), *PpSnRK2AiOX/ProEF1α:D2* (D), and  
723 *PpABI3AiOX/ProEF1α:D2* (E). Times after treatment are indicated. The 12th cells were  
724 observed as the basal cells. Scale bars = 50 μm. Arrowheads indicate cross walls of the  
725 original branches.

726

727 **Figure 2. Dendra2 movement between protonemal cells in transgenic lines**  
728 **overexpressing *PpABI1A*<sup>G333D</sup>, *PpSnRK2A*, or *PpABI3A*.**

729 A and B, Representative differential interference contrast (DIC) and photoconverted Dendra2  
730 fluorescence (gray) images in protonemal cells of *ProEF1α:D2* (A) and  
731 *PpABI1A*<sup>G333D</sup>*OX/ProEF1α:D2* (B) treated with DMSO or ABA. C to E, Representative DIC  
732 and photoconverted Dendra2 fluorescence (gray) images in protonemal cells of *ProEF1α:D2*  
733 (C), *PpSnRK2AiOX/ProEF1α:D2* (D), and *PpABI3AiOX/ProEF1α:D2* (E) treated with  
734 DMSO or β-estradiol. Times after photoconversion are indicated. Scale bars = 100 μm.

735

736 **Figure 3. Quantitative characterization of Dendra2 movement between protonemal cells**  
737 **and its suppression by ABA.**

738 A, Representative DIC, non-photoconverted (green), and photoconverted (gray) Dendra2  
739 fluorescence images in protonemal cells of *ProEF1α:D2* treated with DMSO or ABA. Times  
740 after photoconversion are indicated. Scale bars = 100 μm. B, Mean fluorescence intensity of  
741 Dendra2 at 20-min intervals after photoconversion in photoconverted protonemal cells of  
742 *ProEF1α:D2* treated with DMSO (*n* = 15) or ABA (*n* = 27). Standard deviation (SD) is  
743 indicated by shaded area. The time constant ( $\tau$ ) and immobile fraction (*B*) were determined by

744 fitting the exponential function to the kinetics of mean fluorescence intensity (black solid  
745 lines). RSS, residual sum of squares. C, Schematic diagram of kinetics obtained by using  
746 different combinations of fitting parameters. Intercellular diffusivity of macromolecules is  
747 determined by  $\tau$  and  $B$ . Highly permeable PD allow Dendra2 to move more rapidly from the  
748 original cell (black) than lower permeable PD (blue). More Dendra2 is trapped in the original  
749 cell when immobile fraction is increased (red).

750

751 **Figure 4. Intercellular Dendra2 diffusivity in protonemal cells of**  
752 ***ProEF1 $\alpha$ :D2/ppsnrk2qko* and *ProEF1 $\alpha$ :D2/ppabi3tko*.**

753 A and C, Representative DIC and photoconverted Dendra2 fluorescence (gray) images in  
754 protonemal cells of *ProEF1 $\alpha$ :D2/ppsnrk2qko* (A) and *ProEF1 $\alpha$ :D2/ppabi3tko* (C) treated  
755 with DMSO or ABA. Times after photoconversion are indicated. Scale bars = 100  $\mu$ m. B and  
756 D, Mean fluorescence intensity of Dendra2 at 20-min intervals after photoconversion in  
757 protonemal cells of *ProEF1 $\alpha$ :D2/ppsnrk2qko* (B) and *ProEF1 $\alpha$ :D2/ppabi3tko* (D) treated  
758 with DMSO or ABA with exponential fits to the mean data. SD is indicated by the shaded  
759 area. The  $\tau$  and  $B$  were determined by fitting the exponential function to the kinetics of mean  
760 fluorescence intensity (black solid lines). E to H, Values of the time constant  $\tau$  and  $B$  obtained  
761 through the fittings. The  $\tau$  and  $B$  in *ProEF1 $\alpha$ :D2* and *ProEF1 $\alpha$ :D2/ppsnrk2qko* (E and F), and  
762 in *ProEF1 $\alpha$ :D2* and *ProEF1 $\alpha$ :D2/ppabi3tko* (G and H). Each violin plot shows the density  
763 distribution of the data by the box plot (median as a yellow horizontal line, interquartile range  
764 as a box, and data range as whiskers). The  $P$  value was determined by the Mann-Whitney  
765  $U$ -test. *ProEF1 $\alpha$ :D2* with DMSO ( $n = 17$ ) and ABA ( $n = 24$ ) (E and F), and  
766 *ProEF1 $\alpha$ :D2/ppsnrk2qko* with DMSO ( $n = 13$ ) and ABA ( $n = 22$ ) (B, E and F). *ProEF1 $\alpha$ :D2*  
767 with DMSO ( $n = 15$ ) and ABA ( $n = 27$ ) (G and H), and *ProEF1 $\alpha$ :D2/ppabi3tko* with DMSO  
768 ( $n = 14$ ) and ABA ( $n = 17$ ) (D, G and H). I, Time to initiation of ASD calculated from the  
769 median of fitting parameters in *ProEF1 $\alpha$ :D2* and *ProEF1 $\alpha$ :D2/ppabi3tko*. The grey line  
770 indicates  $A_{90}$ .

771

772 **Figure 5. Live-cell imaging of aniline blue staining for callose after ABA treatment.**

773 A to C, Representative images of DIC and aniline blue fluorescence for callose staining in  
774 protonemal cells of *ProEF1α:D2* (A), *ProEF1α:D2/ppsnrk2qko* (B), and  
775 *ProEF1α:D2/ppabi3tko* (C) after DMSO or ABA treatment. Times after treatment are  
776 indicated. The callose signal is shown in Fire look-up table of ImageJ. Scale bars = 20 μm. D,  
777 Change in aniline blue fluorescence intensity on cross walls in protonemal cells of  
778 *ProEF1α:D2*, *ProEF1α:D2/ppsnrk2qko*, and *ProEF1α:D2/ppabi3tko* after DMSO or ABA  
779 treatment. *ProEF1α:D2* with DMSO ( $n = 12$ ) and ABA ( $n = 12$ ), *ProEF1α:D2/ppsnrk2qko*  
780 with DMSO ( $n = 12$ ) and ABA ( $n = 8$ ), and *ProEF1α:D2/ppabi3tko* with DMSO ( $n = 10$ ) and  
781 ABA ( $n = 12$ ). The  $P$  value was determined by the Welch's  $t$ -test, n.s., non-significance ( $P \geq$   
782 0.05). E to G, Representative images of DIC and punctate callose signal of aniline blue  
783 fluorescence at cross walls between the 11th and 12th cell of *ProEF1α:D2* (E),  
784 *ProEF1α:D2/ppsnrk2qko* (F), and *ProEF1α:D2/ppabi3tko* (G) protonemal cells after ABA  
785 treatment. Times after treatment are indicated. Scale bars = 5 μm. Arrowheads indicate  
786 punctate signals included in the number as an example (E). H, The density of punctate signals  
787 on cross walls between the 11th and 12th cell in *ProEF1α:D2*, *ProEF1α:D2/ppsnrk2qko*, and  
788 *ProEF1α:D2/ppabi3tko* after ABA treatment. Each violin plot shows the density distribution  
789 of the data by the box plot (median as a cyan horizontal line, interquartile range as a box, and  
790 data range as whiskers). *ProEF1α:D2* without and after 20-, 100- and 180-min ABA treatment  
791 ( $n = 19, 17, 18$  and  $30$ , respectively), *ProEF1α:D2/ppsnrk2qko* without and after 20-, 100-  
792 and 180-min ABA treatment ( $n = 18, 8, 9$  and  $9$ , respectively), and *ProEF1α:D2/ppabi3tko*  
793 without and after 20-, 100- and 180-min ABA treatment ( $n = 10, 18, 19$  and  $18$ , respectively).  
794 The  $P$  value was determined by the Mann-Whitney  $U$ -test, n.s., non-significance  $P \geq 0.05$ .

795

796 **Figure 6. Viability under salt stress after different pretreatment time of ABA.**

797 A, Representative bright field, PI and non-photoconverted Dendra2 fluorescence images after  
798 the salt stress treatment. Cells with PI signal indicate dead cells. B, Survival rate after the salt  
799 stress with ABA pretreatment. "w/o NaCl" indicates the condition without salt stress and ABA  
800 treatment. The bar graph shows mean  $\pm$  SD of the survival rate ( $n = 75$ ). The  $P$  value was  
801 determined by the Mann-Whitney  $U$ -test, n.s., non-significance ( $P \geq 0.05$ ),  $*P < 0.01$

802 compared to the non-ABA pretreated corresponding line.

803

804

805 **References**

806 **Amagai A, Honda Y, Ishikawa S, Hara Y, Kuwamura M, Shinozawa A., et al. (2018)**

807 Phosphoproteomic profiling reveals ABA-responsive phosphosignaling pathways in  
808 *Physcomitrella patens*. *Plant J* **94**: 699-708

809 **Amsbury S, Kirk P, Benitez-Alfonso Y (2018)** Emerging models on the regulation of  
810 intercellular transport by plasmodesmata-associated callose. *J Exp Bot* **69**: 105-115

811 **Arif MA, Alseekh S, Harb J, Fernie A, Frank W (2018)** Abscisic acid, cold and salt  
812 stimulate conserved metabolic regulation in the moss *Physcomitrella patens*. *Plant*  
813 *Biol* **20**: 1014-1022

814 **Bedi S, Chaudhuri RN (2018)** Transcription factor ABI3 auto-activates its own expression  
815 during dehydration stress response. *FEBS Lett* **592**: 2594-2611

816 **Brault ML, Petit JD, Immel F, Nicolas WJ, Glavier M, Brocard L., et al. (2019)** Multiple  
817 C2 domains and transmembrane region proteins (MCTPs) tether membranes at  
818 plasmodesmata. *EMBO Rep* **20**: e47182

819 **Brunkard JO, Zambryski PC (2017)** Plasmodesmata enable multicellularity: new insights  
820 into their evolution, biogenesis, and functions in development and immunity. *Curr*  
821 *Opin Plant Biol* **35**: 76-83

822 **Eklund DM, Kanei M, Flores-Sandoval E, Ishizaki K, Nishihama R, Kohchi T., et al.**  
823 **(2018)** An evolutionarily conserved abscisic acid signaling pathway regulates  
824 dormancy in the liverwort *Marchantia polymorpha*. *Curr Biol* **28**: 3691-3699.e3

825 **Fernandez-Calvino L, Faulkner C, Walshaw J, Saalbach G, Bayer E, Benitez-Alfonso Y.,**  
826 **et al. (2011)** Arabidopsis plasmodesmal proteome. *PLoS One* **6**: e18880

827 **Gerlitz N, Gerum R, Sauer N, Stadler R (2018)** Photoinducible DRONPA-s: a new tool for  
828 investigating cell-cell connectivity. *Plant J* **94**: 751-766

829 **Golovina EA, Hoekstra FA, Van Aelst AC (2001)** The competence to acquire cellular  
830 desiccation tolerance is independent of seed morphological development. *J Exp Bot*

831           **52**: 1015-1027

832 **Han X, Kim J-Y** (2016) Integrating hormone- and micromolecule-mediated signaling with  
833           plasmodesmal communication. *Mol Plant* **9**: 46-56

834 **Kawade K, Tanimoto H** (2015) Mobility of signaling molecules: the key to deciphering plant  
835           organogenesis. *J Plant Res* **128**: 17-25

836 **Kawade K, Tanimoto H, Horiguchi G, Tsukaya H** (2017) Spatially different tissue-scale  
837           diffusivity shapes *ANGUSTIFOLIA3* gradient in growing leaves. *Biophys J* **113**:  
838           1109-1120

839 **Khandelwal A, Cho SH, Marella H, Sakata Y, Perroud PF, Pan A., et al.** (2010) Role of  
840           ABA and *ABI3* in desiccation tolerance. *Science* **327**: 546-546

841 **Khraiwesh B, Qudeimat E, Thimma M, Chaiboonchoe A, Jijakli K, Alzahmi A., et al.**  
842           (2015) Genome-wide expression analysis offers new insights into the origin and  
843           evolution of *Physcomitrella patens* stress response. *Sci Rep* **5**: 17434

844 **Kitagawa M, Fujita T** (2013) Quantitative imaging of directional transport through  
845           plasmodesmata in moss protonemata via single-cell photoconversion of *Dendra2*. *J*  
846           *Plant Res* **126**: 577-585

847 **Kitagawa, M. and Fujita, T.** (2015) A model system for analyzing intercellular  
848           communication through plasmodesmata using moss protonemata and leaves. *J. Plant*  
849           *Res.* **128**: 63–72.

850 **Kitagawa M, Tomoi T, Fukushima T, Sakata Y, Sato M, Toyooka K., et al.** (2019) Abscisic  
851           acid acts as a regulator of molecular trafficking through plasmodesmata in the moss  
852           *Physcomitrella patens*. *Plant Cell Physiol* **60**: 738-751

853 **Komatsu K, Nishikawa Y, Ohtsuka T, Taji T, Quatrano RS, Tanaka S., et al.** (2009)  
854           Functional analyses of the *ABI1*-related protein phosphatase type 2C reveal  
855           evolutionarily conserved regulation of abscisic acid signaling between *Arabidopsis*  
856           and the moss *Physcomitrella patens*. *Plant Mol Biol* **70**: 327-340

857 **Komatsu K, Suzuki N, Kuwamura M, Nishikawa Y, Nakatani M, Ohtawa H., et al.**  
858           (2013) Group A PP2Cs evolved in land plants as key regulators of intrinsic desiccation  
859           tolerance. *Nat Commun* **4**: 2219

860 **Koornneef M, Reuling G, Karssen CM** (1984) The isolation and characterization of abscisic  
861 acid-insensitive mutants of *Arabidopsis thaliana*. *Physiol Plant* **61**: 377-383

862 **Kubo M, Imai A, Nishiyama T, Ishikawa M, Sato Y, Kurata T., et al.** (2013) System for  
863 stable  $\beta$ -estradiol-inducible gene expression in the moss *Physcomitrella patens*. *PLoS*  
864 *One* **8**: 13

865 **Lee JY** (2014) New and old roles of plasmodesmata in immunity and parallels to tunneling  
866 nanotubes. *Plant Sci* **221**: 13-20

867 **Levy A, Zheng JY, Lazarowitzl SG** (2015) Synaptotagmin SYTA forms ER-plasma  
868 membrane junctions that are recruited to plasmodesmata for plant virus movement.  
869 *Curr Biol* **25**: 2018-2025

870 **Li JX, Wang XQ, Watson MB, Assmann SM** (2000) Regulation of abscisic acid-induced  
871 stomatal closure and anion channels by guard cell AAPK kinase. *Science* **287**:  
872 300-303

873 **Ma Y, Szostkiewicz I, Korte A, Moes D, Yang Y, Christmann A., et al.** (2009) Regulators  
874 of PP2C phosphatase activity function as abscisic acid sensors. *Science* **324**:  
875 1064-1068

876 **Marella HH, Sakata Y, Quatrano RS** (2006) Characterization and functional analysis of  
877 *ABSCISIC ACID INSENSITIVE3*-like genes from *Physcomitrella patens*. *Plant J* **46**:  
878 1032-1044

879 **Minami A, Nagao M, Ikegami K, Koshiba T, Arakawa K, Fujikawa S., et al.** (2005) Cold  
880 acclimation in bryophytes: low-temperature-induced freezing tolerance in  
881 *Physcomitrella patens* is associated with increases in expression levels of  
882 stress-related genes but not with increase in level of endogenous abscisic acid. *Planta*  
883 **220**: 414-423

884 **Mustilli AC, Merlot S, Vavasseur A, Fenzi F, Giraudat J** (2002) Arabidopsis OST1 protein  
885 kinase mediates the regulation of stomatal aperture by abscisic acid and acts upstream  
886 of reactive oxygen species production. *Plant Cell* **14**: 3089-3099

887 **Nagao M, Minami A, Arakawa K, Fujikawa S, Takezawa D** (2005) Rapid degradation of  
888 starch in chloroplasts and concomitant accumulation of soluble sugars associated with



889 ABA-induced freezing tolerance in the moss *Physcomitrella patens*. J Plant Physiol  
890 **162**: 169-180

891 **Nagao M, Oku K, Minami A, Mizuno K, Sakurai M, Arakawa K., et al.** (2006)  
892 Accumulation of theanderoose in association with development of freezing tolerance in  
893 the moss *Physcomitrella patens*. Phytochemistry **67**: 702-709

894 **Nakashima K, Fujita Y, Kanamori N, Katagiri T, Umezawa T, Kidokoro S., et al.** (2009)  
895 Three Arabidopsis SnRK2 protein kinases, SRK2D/SnRK2.2, SRK2E/SnRK2.6/OST1  
896 and SRK2I/SnRK2.3, involved in ABA signaling are essential for the control of seed  
897 development and dormancy. Plant Cell Physiol **50**: 1345-1363

898 **Nishiyama T, Hiwatashi Y, Sakakibara K, Kato M, Hasebe M** (2000) Tagged mutagenesis  
899 and gene-trap in the moss, *Physcomitrella patens* by shuttle mutagenesis. DNA Res **7**:  
900 9-17

901 **Oldenhof H, Wolkers WF, Bowman JL, Tablin F, Crowe JH** (2006) Freezing and  
902 desiccation tolerance in the moss *Physcomitrella patens*: An in situ Fourier transform  
903 infrared spectroscopic study. Biochim Biophys Acta-Gen Subj **1760**: 1226-1234

904 **Park SY, Fung P, Nishimura N, Jensen DR, Fujii H, Zhao Y., et al.** (2009) Abscisic acid  
905 inhibits type 2C protein phosphatases via the PYR/PYL family of START proteins.  
906 Science **324**: 1068-1071

907 **Perez-Sancho J, Vanneste S, Lee E, McFarlane HE, del Valle AE, Valpuesta V., et al.**  
908 (2015) The Arabidopsis synaptotagmin1 is enriched in endoplasmic reticulum-plasma  
909 membrane contact sites and confers cellular resistance to mechanical stresses. Plant  
910 Physiol **168**: 132-143

911 **Rensing SA, Lang D, Zimmer AD, Terry A, Salamov A, Shapiro H., et al.** (2008) The  
912 *Physcomitrella* genome reveals evolutionary insights into the conquest of land by  
913 plants. Science **319**: 64-69

914 **Rowntree JK, Duckett JG, Mortimer CL, Ramsay MM, Pressel S** (2007) Formation of  
915 specialized propagules resistant to desiccation and cryopreservation in the threatened  
916 moss *Ditrichum plumbicola* (Ditrichales, Bryopsida). Ann Bot **100**: 483-496

917 **Saatian B, Austin RS, Tian G, Chen C, Nguyen V, Kohalmi SE., et al.** (2018) Analysis of a

918 novel mutant allele of *GSL8* reveals its key roles in cytokinesis and symplastic  
919 trafficking in Arabidopsis. BMC Plant Biol **18**: 295

920 **Sadovsky RG, Brielle S, Kaganovich D, England JL** (2017) Measurement of rapid protein  
921 diffusion in the cytoplasm by photo-converted intensity profile expansion. Cell Rep  
922 **18**: 2795-2806

923 **Saruhashi M, Ghosh TK, Arai K, Ishizaki Y, Hagiwara K, Komatsu K., et al.** (2015) Plant  
924 Raf-like kinase integrates abscisic acid and hyperosmotic stress signaling upstream of  
925 SNF1-related protein kinase2. Proc Natl Acad Sci USA **112**: E6388-E6396

926 **Schapire AL, Voigt B, Jasik J, Rosado A, Lopez-Cobollo R, Menzel D., et al.** (2008)  
927 *Arabidopsis* synaptotagmin 1 is required for the maintenance of plasma membrane  
928 integrity and cell viability. Plant Cell **20**: 3374-3388

929 **Schnepf E, Reinhard C** (1997) Brachyocytes in *funaria* protonemate: Induction by abscisic  
930 acid and fine structure. J Plant Physiol **151**: 166-175

931 **Shinozawa A, Otake R, Takezawa D, Umezawa T, Komatsu K, Tanaka K., et al.** (2019)  
932 SnRK2 protein kinases represent an ancient system in plants for adaptation to a  
933 terrestrial environment. Commun Biol **2**: 30

934 **Stevenson SR, Kamisugi Y, Trinh CH, Schmutz J, Jenkins JW, Grimwood J., et al.**  
935 (2016) Genetic analysis of *Physcomitrella patens* identifies *ABSCISIC ACID*  
936 *NON-RESPONSIVE*, a regulator of ABA responses unique to basal land plants and  
937 required for desiccation tolerance. Plant Cell **28**: 1310-1327

938 **Takezawa D, Watanabe N, Ghosh TK, Saruhashi M, Suzuki A, Ishiyama K., et al.** (2015)  
939 Epoxycarotenoid-mediated synthesis of abscisic acid in *Physcomitrella patens*  
940 implicating conserved mechanisms for acclimation to hyperosmosis in embryophytes.  
941 New Phytol **206**: 209-219

942 **Tan TH, Sun YN, Peng XJ, Wu GC, Bao F, He YK., et al.** (2017) *ABSCISIC ACID*  
943 *INSENSITIVE3* is involved in cold response and freezing tolerance regulation in  
944 *Physcomitrella patens*. Front Plant Sci **8**: 1599

945 **Tylewicz S, Petterle A, Marttila S, Miskolczi P, Azeez A, Singh RK., et al.** (2018)  
946 Photoperiodic control of seasonal growth is mediated by ABA acting on cell-cell

947 communication. *Science* **360**: 212-214

948 **Umezawa T, Sugiyama N, Mizoguchi M, Hayashi S, Myouga F, Yamaguchi-Shinozaki K.,**  
949 et al. (2009) Type 2C protein phosphatases directly regulate abscisic acid-activated  
950 protein kinases in *Arabidopsis*. *Proc Natl Acad Sci USA* **106**: 17588-17593

951 **Umezawa T, Sugiyama N, Takahashi F, Anderson JC, Ishihama Y, Peck SC., et al.** (2013)  
952 Genetics and phosphoproteomics reveal a protein phosphorylation network in the  
953 abscisic acid signaling pathway in *Arabidopsis thaliana*. *Sci Signal* **6**: 270

954 **Verkman AS** (2002) Solute and macromolecule diffusion in cellular aqueous compartments.  
955 *Trends Biochem Sci* **27**: 27-33

956 **Vlad F, Rubio S, Rodrigues A, Sirichandra C, Belin C, Robert N., et al.** (2009) Protein  
957 phosphatases 2C regulate the activation of the Snf1-related kinase OST1 by abscisic  
958 Acid in *Arabidopsis*. *Plant Cell* **21**: 3170-3184

959 **Wang PC, Xue L, Batelli G, Lee S, Hou YJ, Van Oosten MJ., et al.** (2013) Quantitative  
960 phosphoproteomics identifies SnRK2 protein kinase substrates and reveals the  
961 effectors of abscisic acid action. *Proc Natl Acad Sci USA* **110**: 11205-11210

962 **Wolkers WF, Alberda M, Koornneef M, Leon-Kloosterziel KM, Hoekstra FA** (1998)  
963 Properties of proteins and the glassy matrix in maturation-defective mutant seeds of  
964 *Arabidopsis thaliana*. *Plant J* **16**: 133-143

965 **Wu S, Koizumi K, MacRae-Crerar A, Gallagher KL** (2011) Assessing the utility of  
966 photoswitchable fluorescent proteins for tracking intercellular protein movement in  
967 the *Arabidopsis* root. *PLoS One* **6**: e27536

968 **Wu SW, Kumar R, Iswanto ABB, Kim JY** (2018) Callose balancing at plasmodesmata. *J*  
969 *Exp Bot* **69**: 5325-5339

970 **Yoshida R, Hobo T, Ichimura K, Mizoguchi T, Takahashi F, Aronso J., et al.** (2002)  
971 ABA-activated SnRK2 protein kinase is required for dehydration stress signaling in  
972 *Arabidopsis*. *Plant Cell Physiol* **43**: 1473-1483

973 **Yoshida T, Christmann A, Yamaguchi-Shinozaki K, Grill E, Fernie AR** (2019) Revisiting  
974 the basal role of ABA - roles outside of stress. *Trends Plant Sci* **24**: 625-635

975 **Yotsui I, Serada S, Naka T, Saruhashi M, Taji T, Hayashi T., et al.** (2016) Large-scale

976 proteome analysis of abscisic acid and ABSCISIC ACID INSENSITIVE3-dependent  
977 proteins related to desiccation tolerance in *Physcomitrella patens*. *Biochem Biophys*  
978 *Res Commun* **471**: 589-595

979 **Zavaliev R, Epel BL** (2015) Imaging callose at plasmodesmata using aniline blue:  
980 quantitative confocal microscopy. *Methods Mol Biol* 1217, 105-119

981 **Zhao MK, Li QL, Chen ZH, Lv Q, Bao F, Wang XQ.**, et al. (2018) Regulatory mechanism  
982 of ABA and ABI3 on vegetative development in the moss *Physcomitrella patens*. *Int J*  
983 *Mol Sci* **19**: 2728

984

985

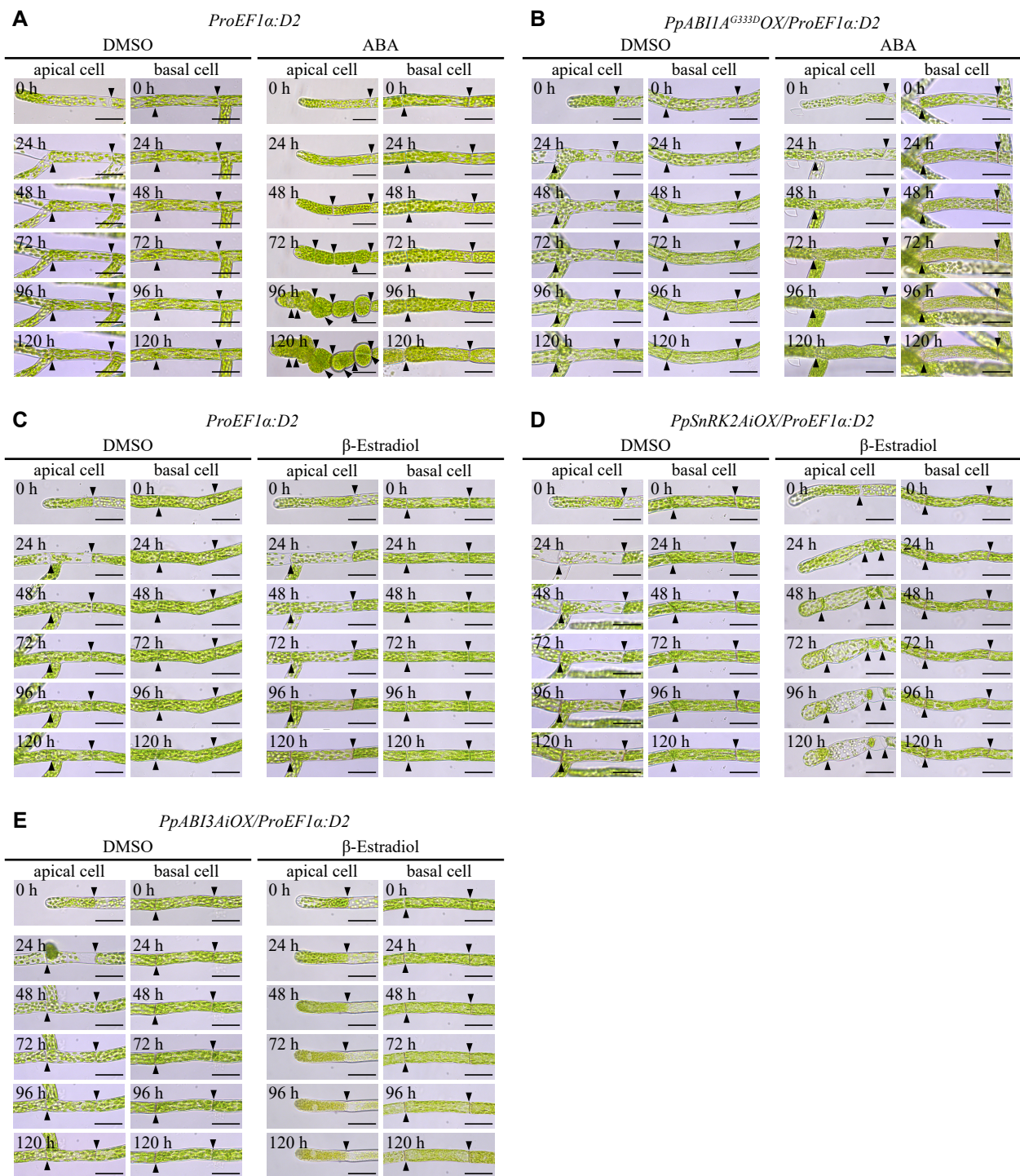


**Figure 1. Morphology and growth of protonemal cells in transgenic lines overexpressing *PpABI1A<sup>G333D</sup>*, *PpSnRK2A*, or *PpABI3A*.**

A and B, Representative images of protonemal cells at apical and basal positions after DMSO or ABA treatment in *ProEF1α:D2* (A) and *PpABI1A<sup>G333D</sup>OX/ProEF1α:D2* (B). C to E, Representative images of protonemal cells at apical and basal positions after DMSO or β-estradiol treatment in *ProEF1α:D2* (C), *PpSnRK2AiOX/ProEF1α:D2* (D), and *PpABI3AiOX/ProEF1α:D2* (E). Times after treatment are indicated. The 12th cells were observed as the basal cells. Scale bars = 50 μm. Arrowheads indicate cross walls of the original branches.

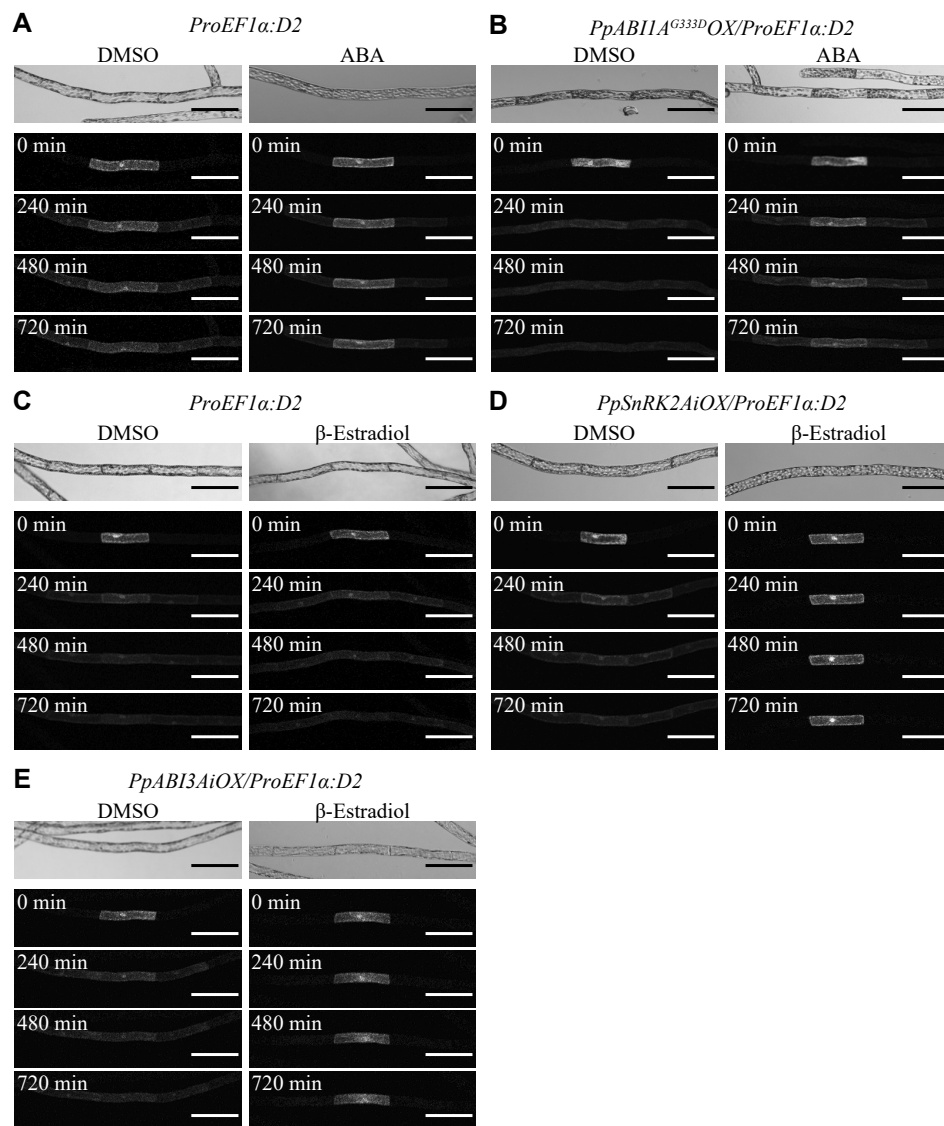


**Figure 2. Dendra2 movement between protonemal cells in transgenic lines overexpressing *PpABI1A*<sup>G333D</sup>, *PpSnRK2A*, or *PpABI3A*.**

A and B, Representative differential interference contrast (DIC) and photoconverted Dendra2 fluorescence (gray) images in protonemal cells of *ProEF1α:D2* (A) and *PpABI1A*<sup>G333D</sup>*OX/ProEF1α:D2* (B) treated with DMSO or ABA. C to E, Representative DIC and photoconverted Dendra2 fluorescence (gray) images in protonemal cells of *ProEF1α:D2* (C), *PpSnRK2AiOX/ProEF1α:D2* (D), and *PpABI3AiOX/ProEF1α:D2* (E) treated with DMSO or β-estradiol. Times after photoconversion are indicated. Scale bars = 100 μm.

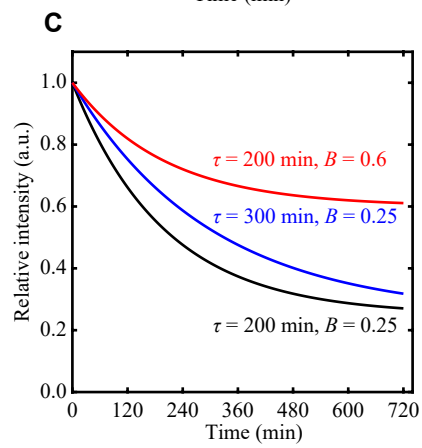
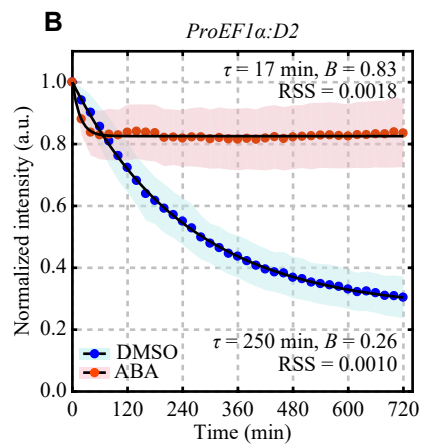
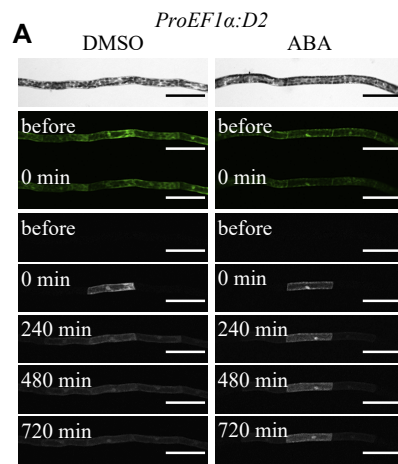


**Figure 3. Quantitative characterization of Dendra2 movement between protonemal cells and its suppression by ABA.**

A, Representative DIC, non-photoconverted (green), and photoconverted (gray) Dendra2 fluorescence images in protonemal cells of *ProEF1 $\alpha$ :D2* treated with DMSO or ABA. Times after photoconversion are indicated. Scale bars = 100  $\mu$ m. B, Mean fluorescence intensity of Dendra2 at 20-min intervals after photoconversion in **photoconverted** protonemal cells of *ProEF1 $\alpha$ :D2* treated with DMSO ( $n = 15$ ) or ABA ( $n = 27$ ). Standard deviation (SD) is indicated by shaded area. The time constant ( $\tau$ ) and immobile fraction ( $B$ ) were determined by fitting the exponential function to the kinetics of mean fluorescence intensity (black solid lines). RSS, residual sum of squares. C, Schematic diagram of kinetics obtained by using different combinations of fitting parameters. Intercellular diffusivity of macromolecules is determined by  $\tau$  and  $B$ . Highly permeable PD allow Dendra2 to move more rapidly from the original cell (black) than lower permeable PD (blue). More Dendra2 is trapped in the original cell when immobile fraction is increased (red).



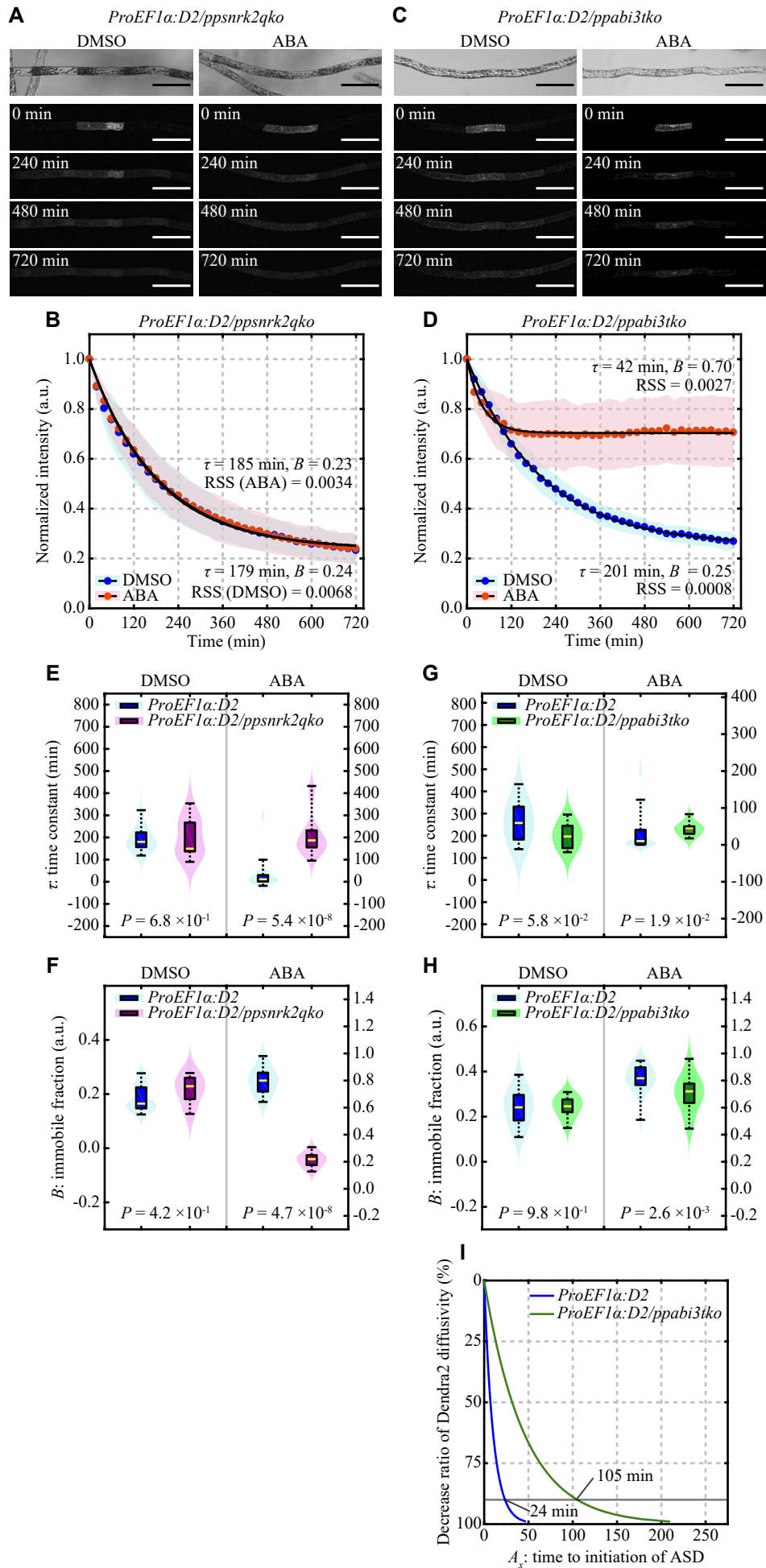


**Figure 4. Intercellular Dendra2 diffusivity in protonemal cells of *ProEF1α:D2/ppsnrk2qko* and *ProEF1α:D2/ppabi3tko*.**

A and C, Representative DIC and photoconverted Dendra2 fluorescence (gray) images in protonemal cells of *ProEF1α:D2/ppsnrk2qko* (A) and *ProEF1α:D2/ppabi3tko* (C) treated with DMSO or ABA. Times after photoconversion are indicated. Scale bars = 100 μm. B and D, Mean fluorescence intensity of Dendra2 at 20-min intervals after photoconversion in protonemal cells of *ProEF1α:D2/ppsnrk2qko* (B) and *ProEF1α:D2/ppabi3tko* (D) treated with DMSO or ABA with exponential fits to the mean data. SD is indicated by the shaded area. The  $\tau$  and  $B$  were determined by fitting the exponential function to the kinetics of mean fluorescence intensity (black solid lines). E to H, Values of the time constant  $\tau$  and  $B$  obtained through the fittings. The  $\tau$  and  $B$  in *ProEF1α:D2* and *ProEF1α:D2/ppsnrk2qko* (E and F), and in *ProEF1α:D2* and *ProEF1α:D2/ppabi3tko* (G and H). Each violin plot shows the density distribution of the data by the box plot (median as a yellow horizontal line, interquartile range as a box, and data range as whiskers). The  $P$  value was determined by the Mann-Whitney  $U$ -test. *ProEF1α:D2* with DMSO ( $n = 17$ ) and ABA ( $n = 24$ ) (E and F), and *ProEF1α:D2/ppsnrk2qko* with DMSO ( $n = 13$ ) and ABA ( $n = 22$ ) (B, E and F). *ProEF1α:D2* with DMSO ( $n = 15$ ) and ABA ( $n = 27$ ) (G and H), and *ProEF1α:D2/ppabi3tko* with DMSO ( $n = 14$ ) and ABA ( $n = 17$ ) (D, G and H). I, Time to initiation of ASD calculated from the median of fitting parameters in *ProEF1α:D2* and *ProEF1α:D2/ppabi3tko*. The grey line indicates  $A_{90}$ .

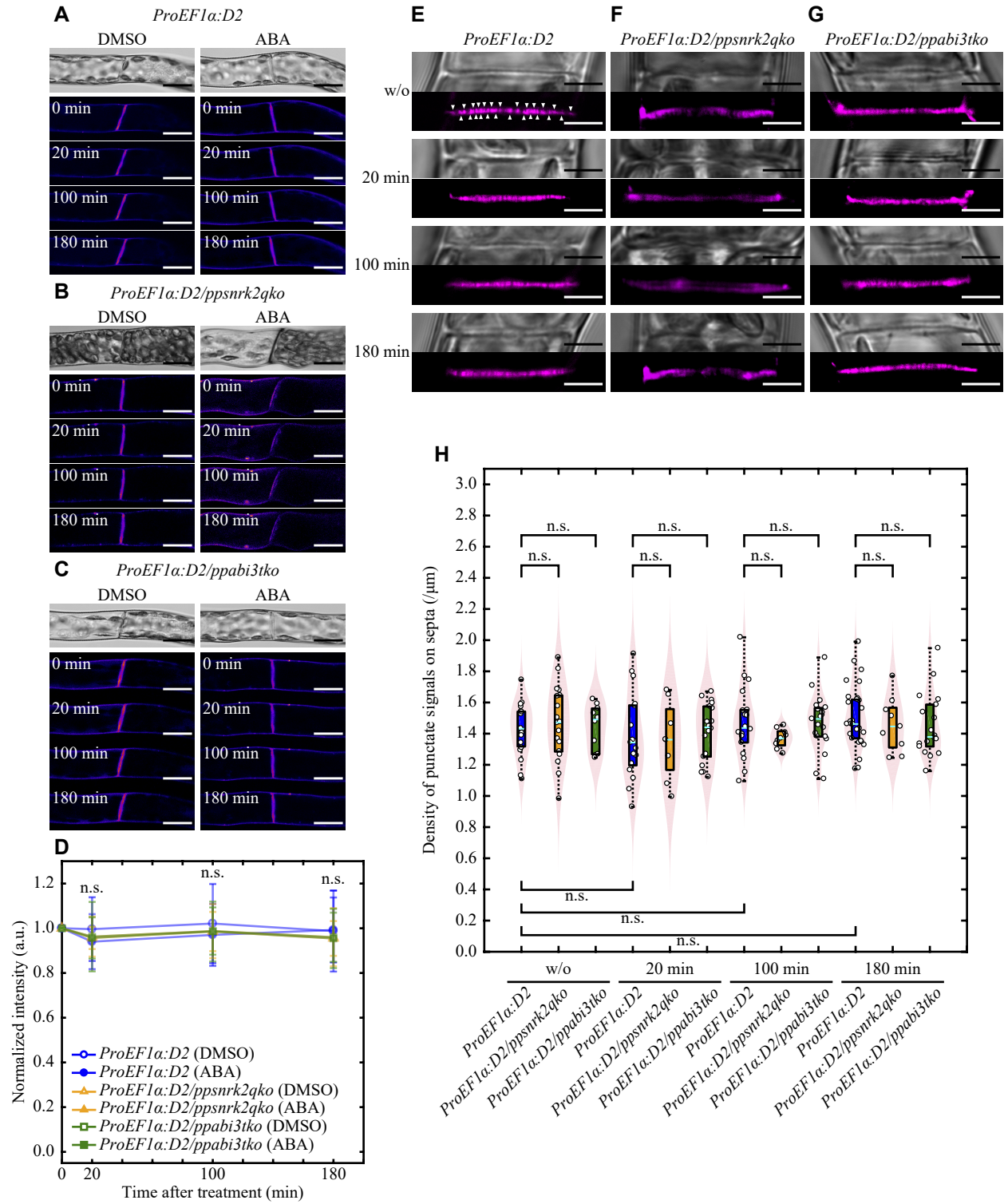


**Figure 5. Live-cell imaging of aniline blue staining for callose after ABA treatment.**

**A and B C**, Representative images of DIC and aniline blue fluorescence for callose staining in protonemal cells of *ProEF1α:D2* (A), *ProEF1α:D2/ppsnrk2qko* (B), and *ProEF1α:D2/ppabi3tko* (C) after DMSO or ABA treatment. Times after treatment are indicated. The callose signal is shown in Fire look-up table of ImageJ. Scale bars = 20 μm. **D**, Change in aniline blue fluorescence intensity on cross walls in protonemal cells of *ProEF1α:D2*, *ProEF1α:D2/ppsnrk2qko*, and *ProEF1α:D2/ppabi3tko* after DMSO or ABA treatment. *ProEF1α:D2* with DMSO ( $n = 12$ ) and ABA ( $n = 12$ ), *ProEF1α:D2/ppsnrk2qko* with DMSO ( $n = 12$ ) and ABA ( $n = 8$ ), and *ProEF1α:D2/ppabi3tko* with DMSO ( $n = 10$ ) and ABA ( $n = 12$ ). The  $P$  value was determined by the Welch's  $t$ -test, n.s., non-significance ( $P \geq 0.05$ ). **D and E E to G**, Representative images of DIC and punctate callose signal of aniline blue fluorescence at cross walls between the 11th and 12th cell of *ProEF1α:D2* (D), *ProEF1α:D2/ppsnrk2qko* (E), and *ProEF1α:D2/ppabi3tko* (F) protonemal cells (E) after ABA treatment. Times after treatment are indicated. Scale bars = 5 μm. Arrowheads indicate punctate signals included in the number as an example (D). **F H**, The number density of punctate signals on cross walls between the 11th and 12th cell in *ProEF1α:D2*, *ProEF1α:D2/ppsnrk2qko*, and *ProEF1α:D2/ppabi3tko* after ABA treatment. Each violin plot shows the density distribution of the data by the box plot (median as a yellowcyan horizontal line, interquartile range as a box, and data range as whiskers). *ProEF1α:D2* without and after 20-, 100- and 180-min ABA treatment ( $n = 19, 17, 18$  and  $30$ , respectively), *ProEF1α:D2/ppsnrk2qko* without and after 20-, 100- and 180-min ABA treatment ( $n = 18, 8, 9$  and  $9$ , respectively), and *ProEF1α:D2/ppabi3tko* without and after 20-, 100- and 180-min ABA treatment ( $n = 10, 18, 19$  and  $18$ , respectively). The  $P$  value was determined by the Mann-Whitney  $U$ -test, n.s., non-significance ( $P \geq 0.05$ ).

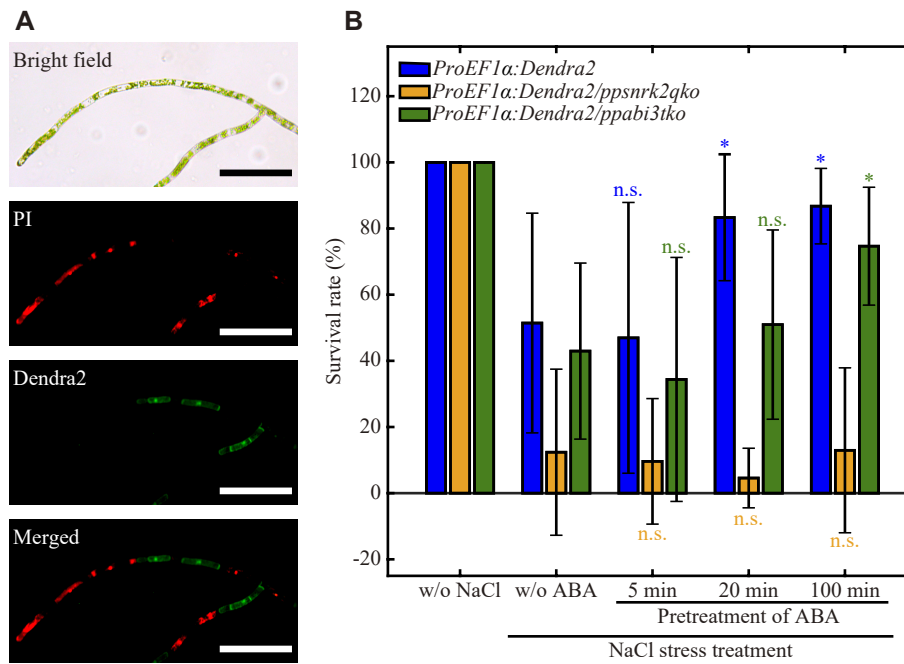


**Figure 6. Viability under salt stress after different pretreatment time of ABA.**

A, Representative bright field, PI and non-photoconverted Dendra2 fluorescence images after the salt stress treatment. Cells with PI signal indicate dead cells. B, Survival rate after the salt stress with ABA pretreatment. “w/o NaCl” indicates the condition without salt stress and ABA treatment. The bar graph shows mean  $\pm$  SD of the survival rate ( $n = 75$ ). The  $P$  value was determined by the Mann-Whitney  $U$ -test, n.s., non-significance ( $P \geq 0.05$ ), \* $P < 0.01$  compared to the non-ABA pretreated corresponding line.